Renewable and Sustainable Energy Reviews 186 (2023) 113666

Contents lists available at ScienceDirect

Renewable and Sustainable Energy Reviews

journal homepage: www.elsevier.com/locate/rser

Mechanistic modelling of catalytic NO_X reduction reactions after hydrogen or ammonia combustion on multiple scales

J. Voglar [a], J. Teržan [a,b], A. Kroflič [a], M. Huš [a,c,d], B. Likozar [a,e,f,g,*]

[a] Department of Catalysis and Chemical Reaction Engineering, National Institute of Chemistry, Hajdrihova 19, 1001, Ljubljana, Slovenia
[b] Department of Synthesis of Materials, Jožef Stefan Institute, Jamova Cesta 39, 1000, Ljubljana, Slovenia
[c] Association for Technical Culture of Slovenia (ZOTKS), Zaloška 65, SI-1000, Ljubljana, Slovenia
[d] Institute for the Protection of Cultural Heritage of Slovenia, Poljanska 40, 1000, Ljubljana, Slovenia
[e] Faculty of Chemistry and Chemical Technology, University of Ljubljana, Večna Pot 113, 1001, Ljubljana, Slovenia
[f] Faculty of Chemistry and Chemical Engineering, University of Maribor, Smetanova Ulica 17, 2000, Maribor, Slovenia
[g] Faculty of Polymer Technology, Ozare 19, SI-2380, Slovenj Gradec, Slovenia

ARTICLE INFO

Keywords:
Hydrogen
Ammonia
Modelling
Selective catalytic reduction
$DeNO_X$

ABSTRACT

This article provides a comprehensive review and evaluation of the selective catalytic reduction (SCR) of nitrogen oxides (NO_X) using ammonia as a reducing agent in flue gases produced by the combustion of hydrogen or ammonia with air. Over the years, density functional theory calculations (DFT) have been used extensively to complement experimental results, with emphasis on understanding adsorption modes and reaction mechanisms. Recent advances in this field have led to a shift from non-periodic to more accurate periodic models. It has been shown that the SCR reactions mainly follow the Eley-Rideal mechanism, with NH_2NO identified as the most important intermediate. Global kinetic and microkinetic models are widely used, but these models often overlook the crucial role of adsorption of water molecules on catalyst surfaces. Consequently, their utility is reduced under conditions of elevated water vapor concentrations. To address this limitation, numerical fluid dynamics simulations (CFD) have been introduced that include user-defined functions to model chemical $deNO_X$ reactions. In particular, the method CFD can also take into account the adsorption of relevant species at the active sites of the catalyst. We highlight a significant knowledge gap in the existing literature: the lack of consideration of the adsorption of water on catalyst surfaces during the selective catalytic reduction of NO_X. Consequently, these models are inadequate for flue gases with high water vapor content produced during the combustion of hydrogen or ammonia. Addressing this shortcoming is critical to better understand and accurately predict the performance of SCR under different operating conditions.

1. Introduction

The transition to a carbon-neutral society requires the decarbonization of the high-temperature heating used in many sectors (e.g. process metallurgy) [1,2], which can only be achieved by using carbon-neutral (synthetic fuels and biofuels) or carbon-free fuels. Two of the most promising carbon-free fuels are hydrogen (H_2) [3,4] and ammonia (NH_3) [5,6]. These two fuels can be used for transportation and electricity generation: H_2 has proven to be a fuel for internal combustion engines [7–10], as has a mixture of NH_3 and H_2 [11,12]; gas turbines can run on pure NH_3 [13], its mixture with H_2 [14] and on pure H_2 [15]. None of the fuels, neither H_2 nor NH_3, emit carbon dioxide or carbon monoxide during its combustion. However, combustion with air produces NO_X emissions (a mixture of nitrogen oxide (NO) and nitrogen dioxide (NO_2) [16]; see Appendix A), which pose an environmental and health hazard.

Among other things, NO_X contributes to the formation of acid rain, which is responsible for the eutrophication of soils and water bodies and has negative effects on aquatic ecosystems as well as terrestrial vegetation [17]. Although acidic nitrate/nitric acid particles have not been shown to have direct effects on the human health [18], NO and NO_2 gases irritate the respiratory tract and cause respiratory issues via inflammation and cell damage. This makes NO_x one of the priority air pollutants for which limit values for the protection of the human health, vegetation and natural ecosystems are laid down in various directives (e.g. Directive 2008/50/EC on ambient air quality and cleaner air for Europe). Direct exposure to the more acutely toxic NO_2 can lead to

* Corresponding author.Department of Catalysis and Chemical Reaction Engineering, National Institute of Chemistry, Hajdrihova 19, 1001, Ljubljana, Slovenia.
E-mail address: blaz.likozar@ki.si (B. Likozar).

https://doi.org/10.1016/j.rser.2023.113666
Received 19 May 2023; Received in revised form 18 August 2023; Accepted 18 August 2023
Available online 25 August 2023

Abbreviations

3D	three-dimensional
CFD	computational fluid dynamics
CHA	chabazite
deNO$_X$	denitrification
DFT	density functional theory
DOC	diesel oxidation catalyst
DRIFTS	diffuse reflectance infrared Fourier transform spectroscopy
EPR	electron paramagnetic resonance
ER	Eley-Rideal mechanism
ER	equivalence ratio
FTIR	Fourier-transform infrared spectroscopy
GGA	generalized gradient approximation
H_2	molecular hydrogen
H_2O	water
IR	infrared
LDA	local density approximation
LH	Langmuir-Hinshelwood mechanism
LNT	lean NO$_X$ traps
MOFs	metal-organic frameworks
N_2	molecular nitrogen
N_2O	nitrous oxide
NH_3	ammonia
nitro-PAHs	nitroaromatic and nitrated polyaromatic hydrocarbons
NO	nitrogen oxide (nitric oxide)
NO_2	nitrogen dioxide
NO$_X$	nitrogen oxides
NTPRD	non-thermal plasma reduction
PMoA	phosphomolybdic acid
R&D	research and development
SCR	selective catalytic reduction
SNCR	selective non-catalytic reduction
SO_2	sulfur dioxide
UDF	user-defined function
UV	ultraviolet
UWS	urea-water solution
VOCs	volatile organic compounds
XPS	X-ray photoelectron spectroscopy
XAS	X-ray absorption spectroscopy
XRD	X-ray diffraction
ZSM	zeolite Socony Mobil

respiratory inflammation and reduced lung function (e.g. asthma) and increase susceptibility to other respiratory infections already at low-ppm levels [19]. However, NO$_X$ is also harmful because of its indirect effects on the ecosystem, human health and climate. Photolysis of NO_2 leads to the formation of toxic ozone in the lower atmosphere and, in combination with volatile organic compounds (VOCs), to the formation of photochemical smog, which is particularly harmful to health [20], but also reduces visibility and contributes to climate change. Nitrogen oxide species in the atmosphere react with other air pollutants to form, for example, nitroaromatic and nitrated polyaromatic hydrocarbons (nitro-PAHs), which are highly toxic, carcinogenic and mutagenic to humans and other living organisms [21–23]. In particular, nitrated (poly)aromatic pollutants are also strong absorbers of the near UV radiation and visible light, which causes atmospheric heating and climate change [24].

Therefore, in addition to decarbonization, there is a global need to reduce the combustion emissions of NO$_X$ into the atmosphere, including emissions from the combustion of ammonia and/or hydrogen (with air), which can be achieved by selective catalytic reduction of nitrogen oxides (SCR deNO$_X$). Alternative ways to reduce nitrogen oxide emissions include avoiding their formation during combustion through (i) oxyfuel combustion (combustion in a near-pure oxygen environment) [25,26], (ii) optimized burner design and proper combustion management [15,27,28] and (iii) catalytic combustion e.g. catalytic hydrogen combustion (CHC) [29]. Examples of alternative post-combustion reduction technologies include (i) selective non-catalytic reduction (SNCR), which includes the injection of a reagent at high temperatures (between 850 and 1175 °C) [30,31], (ii) NO$_X$ storage in lean NO$_X$ traps (LNT), which includes NO$_X$ reduction during the periods of rich exhaust gas conditions typically used with hydrocarbon fuels, e.g. diesel [32,33] and (iii) NO$_X$ removal by non-thermal plasma reduction (NTPRD), which necessitates electrical power source to operate [34,35]. However, these alternative NO$_X$ emission reduction methods involve high operating costs (oxyfuel combustion), require research and development (R&D) and investments for infrastructure modifications (optimized or catalytic combustion), or are not applicable to carbon-free fuels (LNT).

1.1. Formation and selective catalytic reduction of nitrogen oxides

During combustion, nitrogen from the air (or the fuel itself) can be converted into nitrogenous pollutants such as NO, NO_2, N_2O, NH_3. The species formed and their ratios depend on the combustion conditions, e.g. temperature, air-to-fuel ratio, pressure, etc. N_2O emissions are usually insignificant because N_2O reacts rapidly with the H and OH radicals to form N_2 or decomposes by itself in colder regions downstream of the flame [16]. On the other hand, the formation and decomposition processes of NO$_X$ during combustion are very complex. There are three different pathways of the NO formation: (i) oxidation of atmospheric nitrogen (with O, O_2 and OH; the Zeldovich mechanism) - thermal NO, (ii) reactions of atmospheric nitrogen with hydrocarbon radicals (mainly HCN; described by Fenimore) - prompt NO and (iii) oxidation of nitrogen bound in the fuel (with O_2; Pershing and Wendt) - fuel NO [16]. NO_2 forms from NO, which usually occurs in the areas, where rapid cooling takes place (e.g. in the area where hot combustion gases mix with the inlet air [16]). Typically, NO$_X$ emissions in the combustion products consist of 90 vol% NO and 10 vol% NO_2 [36].

SCR deNO$_X$ is a process of converting NO$_X$ from flue gases to nitrogen (N_2) and water vapor using a reducing agent and a catalyst. The most commonly used reducing agents for the SCR deNO$_X$ process are NH_3 and urea-water solution (UWS). Alternative reducing agents for SCR deNO$_X$ are: H_2 [37], hydrocarbons, alcohols, carbon monoxide [38] and others. Since most of the research and development work is concentrated on SCR deNO$_X$ with ammonia (NH_3-SCR deNO$_X$), this paper focuses on these processes.

There are three main SCR deNO$_X$ reactions with ammonia in a lean environment (excess oxygen during combustion, which is also present in a flue gas).

$$NH_3 + NO + \frac{1}{4}O_2 \rightarrow N_2 + \frac{3}{2}H_2O \quad (1.1)$$

$$NH_3 + \frac{1}{2}NO + \frac{1}{2}NO_2 \rightarrow N_2 + \frac{3}{2}H_2O \quad (1.2)$$

$$NH_3 + \frac{3}{4}NO_2 \rightarrow \frac{7}{8}N_2 + \frac{3}{2}H_2O \quad (1.3)$$

The reaction (1.1) is usually referred to as the standard SCR reaction. The fastest and preferred SCR reaction is reaction (1.2). To promote reaction 1.2 (rapid SCR reaction), the molar ratio between NO and NO_2 should be close to one. Since NO usually predominates, this could be achieved by pre-oxidizing a portion of NO to NO_2 (using a separate catalyst, e.g. diesel oxidation catalyst (DOC), or on the SCR deNO$_X$

catalyst itself [39]). The reaction 1.3 (NO_2-SCR reaction) occurs when excess NO_2 is present. NO_2 can also react (reaction 1.4) to form N_2O, which is an undesirable side reaction between ammonia and NO_2 because the resulting N_2O has a greenhouse effect and depletes the stratospheric ozone layer [40].

$$NH_3 + NO_2 \rightarrow \frac{1}{2}N_2 + \frac{1}{2}N_2O + \frac{3}{2}H_2O \quad (1.4)$$

Insufficient mixing, excess ammonia, or a rapid release of the stored ammonia (through the catalyst) can cause ammonia emissions, which is known as an ammonia slip. This becomes a problem when high NOx conversions (>90%) are required. Therefore, ammonia slip catalysts (ASC) are commonly used in vehicle exhaust treatment systems to oxidize excess ammonia to harmless nitrogen and water vapor [40].

The presence of SO_2 and/or water vapor in exhaust gases inhibits SCR deNO_X processes due to the effect of SO_2 and H_2O poisoning [41,42]. Hydrogen and ammonia are sulfur-free and the deNO_X catalysts are not poisoned by SO_2. However, water vapor would be present in large quantities. Stoichiometric combustion of hydrogen and ammonia with air produces flue gases with 34.7 vol% and 31.1 vol% water vapor, respectively (Appendix B: Tables B.1 and B.2). Even if the equivalence ratio is increased to 1.25 (lean combustion), the combustion products would contain 28.8 vol% and 26.3 vol% water vapor, respectively.

1.2. Water vapor inhibition effects on the NH_3-SCR deNO_X processes

There are two main mechanisms of the H_2O-induced inhibition of the NH_3-SCR deNO_X reactions and the corresponding catalyst poisoning. The first is hydroxylation of the catalyst surface in the presence of large amounts of water, which reduces the number of available active sites on the catalyst. This is an irreversible process during catalyst operation, as activity is only restored at dehydration temperatures above 350 °C. Moreover, the competing adsorption of H_2O and NH_3 decreases the adsorption capacity for NH_3, which lowers the reaction rate and inhibits the deNO_x process SCR [43].

Some authors [44,45] claim that the inhibition of SCR deNO_X by water vapor is proportional to the water vapor content up to 5 vol% and then flattens out, as shown in Fig. 1.

Yun and Kim [46], on the other hand, have predicted a significant reduction in the NH_3-SCR deNO_X performance of a commercial V_2O_5 catalyst even at higher water vapor content, which is shown in Fig. 2. These discrepancies could originate from the differences in experimental

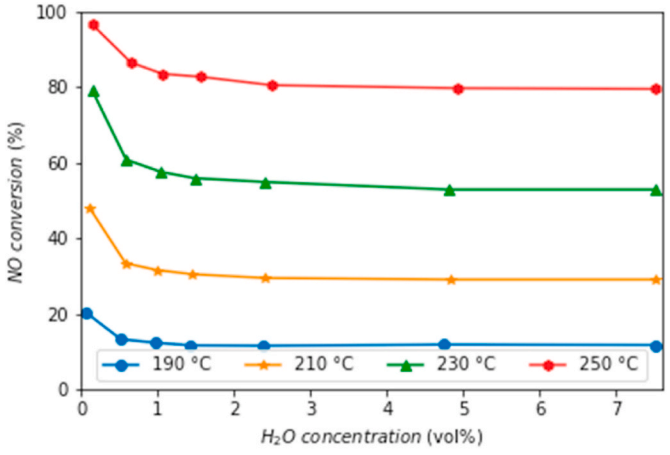

Fig. 1. Effect of water vapor on NO conversion over vanadia-based commercial catalyst (ZERONOX®, Katalysatorwerke HiJls GmbH; 0.4 g of catalyst at 180–300 μm sieve fraction) at various temperatures. Adapted from Ref. [44]. Feed gas mixture: 10 vol% O_2, 1000 ppm NO, 1000 ppm NH_3, 0 to 7.5 vol% H_2O, balance N_2 at flow rate of 500 ml/min. Copyright © 1996 Published by Elsevier Ltd.

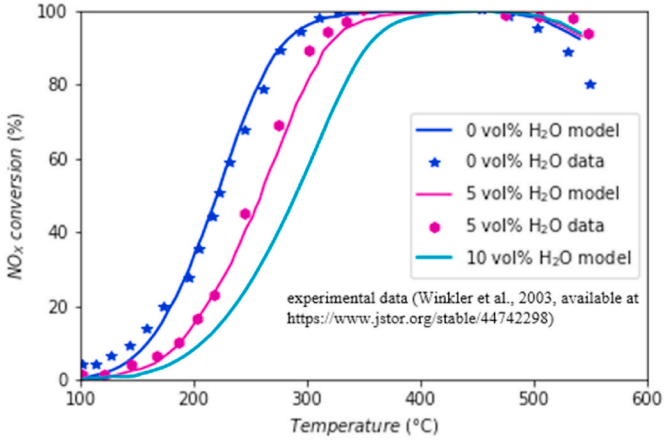

Fig. 2. Influence of H_2O content on the NO_X conversion of a commercial V_2O_5 catalyst (the sample with diameter and length of 1 inch including a 400/4 [cpsi/mil] substrate coated with a vanadium-based washcoat). Adapted from Ref. [46]. The exhaust gas contained 2 vol% O_2, 500 ppm NO and 500 ppm NH_3, H_2O concentration was varied; It was fed to the SCR catalyst at the space velocity of 20,000 h^{-1}. Copyright © 2012 Elsevier Ltd.

conditions: simulated flue gas composition, composition and form (powder versus monolith) of a catalyst sample, pretreatment procedure of gases (e.g. preheating, mixing), sampling and characterization of gases and others.

However, most authors tested catalysts only at low water vapor concentrations in flue gases, usually below 5 vol% [47] and occasionally up to 10 vol% in simulated flue gases [48]. Therefore, the effect of water vapor on the NO_X conversion efficiency at high water content (>15 vol %) is currently unknown.

On the other hand, water vapor may also have a promoting effect on NH_3-SCR deNO_X performance under certain conditions (at H_2O contents below 5 vol%). It can inhibit N_2O formation (enhanced N_2 selectivity), catalyse the transition from Lewis acid sites to Brønsted acid sites and facilitate the production of SCR-reactive intermediates [49]. Both, the promoting and inhibiting effect of H_2O coexist, and the overall effect depends on the water vapor concentration.

1.3. Catalyst materials, characterization and measurement methods

It is difficult to identify the best catalyst for a process as there is usually no single catalyst that gives optimal results under all operating conditions. Therefore, over the years, numerous catalytic materials have been investigated for their activity (and stability) in SCR deNO_X. In the past, commercial SCR deNOx catalysts used to be based on noble metals, such as Rh, Pt and Pd on a metal oxide matrix support (CeO_2, ZrO_2, Al_2O_3 and others) [50]. Current catalytic materials are based on either (i) metal oxides of copper, nickel, iron, vanadium and other transition metals or on (ii) metal ion-exchanged zeolites, mainly Cu- and Fe-exchanged zeolites [51]. Recently, a patent has been published (WO 2019/166267) using a zeolite-based material loaded with iron. Also, the commercial material REMEDIA® has been shown to remove dioxins and NO_X [52]. In some cases, copper-loaded vanadia and TiO_2 materials have also been used for NO_x abatement [50,53,54]. In recent years, increased attention has been given to Mn-based materials [55–57], since several issues plague the vanadium-based catalyst. Since the materials require a higher operating temperature, they are installed up-stream of the exhaust. The latter leads to several issues, such as deactivation of the materials due to coke deposition, poisoning by SO_2, etc. [58].

There are several material properties that determine the catalyst performance. These are usually input data for modelling and predictive studies and must be accurately selected and determined to obtain reliable computational results. The number of active sites and their surface

distribution are essential information for kinetic studies. However, any additional experimental information (e.g. the strength of reactant binding, different types of active sites) drastically improves the accuracy of the developed model.

There are numerous characterization techniques that are ubiquitous in catalyst research, such as powder X-ray diffraction (XRD) and sorption of probe molecules (e.g. N_2, H_2 and CO) [59–61]. These methods provide general information about the catalyst structure (crystallinity) and its surface, which is necessary for the development of a microkinetic model. A very useful complementary technique is chemisorption of reactants, which can provide specific information about the active phase of the catalyst, including the binding strength of reactants and/or products. Competitive adsorption of potential spectator molecules of catalyst poisons is also an important approach, that can be used to evaluate the effect of a poison on catalyst activity [60,62,63]. The amount and the inferred nature of binding provide essential information about the poisoning effect, which is often a bottleneck in catalyst selection. In this regard, X-ray photoelectron spectroscopy (XPS) and diffuse reflectance infrared Fourier transform spectroscopy (DRIFTS) provide complementary information about the binding of molecules and their chemical environment, especially with respect to the oxidation state of the active site. Another very accurate technique that is not widely available is X-ray absorption spectroscopy (XAS). This technique can be used to study the active site at the atomic level, which in combination with DFT calculations can lead to improvements in determining the reaction mechanism [64].

There are many other analytical techniques used in the characterization of catalysts, which have already been described in detail in another review [65]. We mention here only those most commonly used in SCR deNO_x research and would like to emphasize that a combination of different characterization techniques and catalytic tests gives the most accurate results. In this context, a post-mortem catalyst analysis with Mössbauer spectroscopy combined with electron paramagnetic resonance (EPR) used by Grünert et al. [66], has shown that Fe^{III} are the most active sites for NO_x abatement.

1.4. Outline of the paper

This paper is a review of recent advances in the field of mechanistic modelling of SCR of NO_X emissions from flue gases, with emphasis on the treatment of flue gases produced during the combustion of hydrogen or ammonia. The article consists of (i) an introduction explaining the problems associated with nitrogen oxide emissions and methods to reduce them, focusing on NH_3-SCR deNO_X and a description of typical catalyst materials, their characterization and methods to evaluate their performance, (ii) an overview of the SCR deNO_X models at the atomistic scale, (iii) a description of global kinetic and microkinetic models, (iv) a description of SCR catalysis by computational fluid dynamics (CFD), (v) conclusions with a brief summary of the current state of research on the models and a future outlook.

2. Atomistic-scale DFT modelling

Due to the complexity of the reaction network in SCR deNO_X reactions, few first-principles reaction models have been established and investigated using DFT calculations. More often, a reaction mechanism is postulated and experimental data are fitted using microkinetic models that provide phenomenologically optimized kinetic parameters. DFT calculations are mostly used to support experimental data and are limited to adsorption energies, charge transfer and structural properties. The notorious problem remains model construction, which must be computationally tractable, yet physically meaningful. Conventional characterization methods, such as XRD, XPS, IR spectroscopy etc. are used to obtain information about the structure of the material, which is then used as input in modelling.

Structure-activity relationships are highly sought after in the optimization of SCR catalysts. In this chapter, we give an overview of the few first-principles attempts to describe these reactions. Although there are several variants of DFT, computational feasibility and chemical accuracy have reduced the useful approaches to a handful. The generalized gradient approximation (GGA) is most commonly used because it is not much more costly than the local density approximation (LDA) but considerably more accurate. To account for *d* electrons of Ti and V, the Hubbard-like DFT+U approach is usually used. Hybrid-functional realizations of DFT are used only for single point calculations on pre-optimized structures due to their extreme computational costs, although they provide superior electronic properties, very accurate adsorption energies and reaction barriers. Even more expensive methods, such as coupled clusters, are used only to evaluate the accuracy of different lower-level approaches on isolated species, such as on $O{=}V(OH)_3$ and $O{=}VSi_7O_{12}H_7$ [67]. In all cases, periodic calculations are preferred to describe heterogeneous catalysts with a repeating structure. Depending on the purpose of the DFT calculations, different quantities are calculated: (i) geometrical structures, (ii) electronic properties, (iii) adsorption strength, (iv) reaction kinetic parameters. Most simulations focus on (i) and (iii) and consider (ii) only indirectly, while (iv) is almost completely disregarded.

2.1. Structure and electronic properties

Although this is a prerequisite for any DFT calculation, in this section we explicitly list the works where the calculation of the structure and electronic properties is the most important insight offered by DFT. This is usually done to support FTIR, DRIFTS or Raman measurements, or to compare charge transfer and similar quantities with observed reaction performance. Therefore, these studies remain descriptive.

2.1.1. Ceria-based catalysts

Yan et al. [68] investigated Nb-modified SnO_2–CeO_2 catalysts and used DFT calculations to determine the charge distribution and partial electronic charge on the catalyst surfaces as well as the band structures. They also investigated the energy of oxygen vacancy formation. Similarly, Mu et al. used DFT to study the charge interaction between Fe and V in $FeVO_4$ [69].

Nolan et al. focused on the electronic structure and molecular adsorption of NO_2 and O_2 on ceria with different oxygen oxidation numbers [70–72]. Joshi et al. further demonstrated the positive effect of tungsten doping [73].

2.1.2. TiO_2-based catalysts

To support the DRIFTS measurements, Huan et al. also calculated the adsorption of NO, NH_3, NO_2, O_2 and N_2 on TiO_2(001) and TiO_2(101) [74]. Experimental studies on Sm and Zr doping of MnO_x-TiO_2 catalysts were elaborated by Sun et al. [75] using DFT to calculate differential charge densities or deformation electron density and the density of states during adsorption [76]. For MnO_x-FeO_y nanocage catalysts, Yan et al. [77] used DFT only to evaluate the charge density transfer.

Occasionally, DFT simulations are used in design studies, as shown by Peng [78], who calculated the electronic properties of differently doped TiO_2 to evaluate its redox potential. Very rarely, authors use DFT models to explain Raman spectra, as Due-Hansen et al. did for vanadia-based catalysts on wolframated and sulphated zirconia [79].

2.2. Adsorption

Historically, adsorption has been the most common DFT result, such as in the seminal work by Yin et al., in 1999 [80]. Nowadays, adsorption is most often evaluated to explain the experimental data characterizing a catalyst, to provide clues about the reaction mechanism and/or the intermediates involved, or to study the catalyst poisoning. In general, authors calculate the adsorption energies, omitting entropy effects and foregoing the analysis of the Gibbs free energy of adsorption (except

when studying phase diagrams). Therefore, the adsorption energy calculations are used to make comparisons and show trends, but not to predict the catalyst coverage at different operating conditions. This is understandable since the exact catalyst surface area is often unknown or too variable to be suitable for DFT.

2.2.1. Ceria-based catalysts

Peng et al. [81] studied NH_3 adsorption on differentially doped (Fe, Mn, La, Y) CeO_2 catalysts and found that it improved with all dopants. The inherent limitations of modelling are perhaps best illustrated by Maitarad et al. [82], who used to CeO_2(110) and Mn@CeO_2(110) to describe the $MnO_x/Ce_{0.9}Zr_{0.1}O_2$ material while investigating NH_3 adsorption energies and oxygen vacancy formation energies.

Sulfur poisoning of CeO_2 was attributed to the formation of SO_x surface species [83], which is also true for Mn-doped CeO_2 [84]. In the latter case, the authors performed an extensive DFT study, including first-principles phase diagram calculation, which is rarely done, e.g. for Cu-SSZ-13 by Kerkeni et al. [85].

2.2.2. TiO_2-based catalysts

More extensive studies, such as that of Huang et al. [74] on TiO_2(001) and TiO_2(101), investigate the adsorption of several gases involved: NH_3, NO, NO_2, N_2, O_2. Except for NH_3, all other gases were found to be purely physisorbed.

Cheng et al. used DFT, to evaluate the adsorption energy of ammonia on Nb-promoted iron titanate and explain the results of DRIFTS [86]. Similarly, Liu et al. [87] investigated the adsorption of NH_3 and NO on Fe_2O_3/TiO_2{001} and Fe_2O_3/TiO_2{101} and confirmed the superior activity of TiO_2{001}, while Song et al. investigated monomeric vanadium oxide supported anatase (TiO_2) [88]. Since water desorption is often the rate-determining step, several studies focused exclusively on water adsorption, e.g. by Broclawik [89] on W-doped $V_2O_9H_8$ clusters.

One of the few deactivation studies using DFT [90] showed that arsenic-induced poisoning of a commercial catalyst (V_2O_5–WO_3/TiO_2) was due to the formation of unreactive As–OH groups. DFT was used to calculate adsorption energies and charge transfer.

Conversely, Yu et al. [91] showed that SO_2 has a positive effect on Pb-poisoned V_2O_5-WO_3/TiO_2, which they confirmed by calculating SO_2 and NH_3 adsorption on the surface. Peng et al. studied NH_3 adsorption on pristine TiO_2, Mn-substituted TiO_2 and K-doped TiO_2 to evaluate the effects of poisoning [92] and discovered that it was due to the decrease in surface acidity, loss of reducibility and the enhancement of stable nitrite/nitrate species. Similarly, V_2O_5/TiO_2 catalysts doped with MoO_3 and WO_3 were tested for As poisoning [93].

2.2.3. Zeolite-based and other catalysts

The adsorption and dissociation energies of NH_3, including NO- and O_2-assisted pathways, were calculated by Paolucci on Cu-SSZ-13 and compared with operando spectroscopy measurements [94]. The position and oxidation state of the Cu atom in SSZ-13 was then studied in more detail by Borfecchia et al. [95]. Cu-SSZ-13 has been investigated in countless DFT studies, but most of them involved structural calculations with non-periodic [96–105] or periodic models [106–109]. Similarly, MOFs can also act as catalysts, which led Zhang et al. to investigate the adsorption of the involved gases in Mn-MOF-74 [110].

Chen et al. described $Co_{0.5}Mn_1Fe_{0.25}Al_{0.75}O_x$-LDO as $CoMn_2O_4$ (311) when evaluating adsorption energies of NH_3, NO and NO_2 [111]. In PMoA clusters, co-adsorption interactions are important, as shown by Jia et al. [112].

Fan et al. [113] discovered new active sites for SCR on the (001) facet of α-Mn_2O_3, which is more active than the traditional (111) facet. DFT confirmed this is caused by charge redistribution on the surface, which facilitates the adsorption of NH_3 on the (001)-Mn3-terminated surface. MnFeOx nanostructures, such as Dy-doped nanowires [114] or Nb- and Nd-doped nanobelts [115], are also active in SCR due to their strong adsorption of NH_3, as shown by DFT calculations and charge difference analysis.

2.3. Reaction mechanism

Studies of the reaction mechanism are somewhat less common and are usually purely theoretical studies with little to no experimental support. The first study that explicitly investigated the reaction mechanism by calculating transition states was done in 2003, when Anstrom et al. constructed a $V_4O_{16}H_{12}$ cluster to simulate the V_2O_5(010) surface [116]. It was found that NH_4 and NO react to form NH_3NHO, convert to NH_2NO by transferring two hydrogen atoms to the V═O groups and isomerise to various NH_2NO species (NH_2NO, *trans*-NH═NOH, *cis*-NH═NOH, *cis*-HN═NO-*trans*-H). The rate of the SCR reaction is determined by the formation of NH_2NO and not its isomerization. Soyer et al. studied a similar mechanism on a $V_2O_9H_8$ cluster representing V_2O_5(010) [117].

2.3.1. TiO_2-based catalysts

In 2005, Vittadini estabilised one of the first periodic models and described the reaction on TiO_2(001) [118]. The study by Calatayud et al. is noteworthy because it calculated the whole mechanism on different vanadium oxide clusters and periodic models of vanadium-substituted TiO_2(001), considered the reoxidation of the catalyst and compared the results with experiments [119].

Arnarson et al. [120] studied the reaction mechanism with DFT on VO_x/TiO_2(001) catalysts (Fig. 3), including the standard and the fast catalytic reduction reactions. In both cases, NH_3 binds to a V^{5+} active site and reacts with NO. Both cycles (NO-activation and fast SCR) play an important role and have the same reduction part but differ in the active oxidant (NO_2 or NO + O_2). At low temperatures, the standard reaction rate of SCR is determined by the formation and desorption of H_2O. The fast SCR reaction employs NO_2 directly, making the conversion faster. At higher temperatures, the reaction rates are determined by the reduction, which is the same for both pathways. While Arnarson et al. used isolated V species on titanium dioxide, He et al. [121] showed that the use of polymeric vanadyl species improves the catalyst activity due to lower reaction barriers and a smaller number of reaction steps. In all cases, no higher level modelling was performed and only DFT was used to arrive at conclusions. In their seminal work, He et al. [121] showed experimentally and theoretically with full mechanistic evaluation that polymeric vanadyl species are superior to monomeric vanadyl species.

On MnOx/TiO_2, Wei et al. analyzed the three reaction steps: reaction at the Lewis acid site, reaction at the Brønsted acid site and regeneration (oxidation) of the catalyst [122], which are shown in Fig. 4.

Yuan et al. constructed various V_2O_5-based catalytic surfaces and calculated three complete mechanisms: the Lewis acid mechanism, the Brønsted acid mechanism and the nitrite mechanism [123]. They confirmed that the latter two mechanisms compete with each other, while the Lewis acid mechanism does not match experimental observations in terms of the reaction order.

2.3.2. Zeolite-based catalysts and metal-organic frameworks

On Fe-exchanged zeolites, Li and Li investigated the possible reaction mechanism for the rapid SCR reaction using DFT [124]. When investigating the reaction of NO and NO_2 (bound as N_2O_3) with NH_3 in (i) the gas phase and (ii) on zeolites and (iii) the decomposition of NH_4NO_2, the reaction barrier was calculated to be 22.5, 24.0 and 21.2 kcal/mol, respectively. Therefore, Chen et al. focused on oxygen dissociation via $(NH_3–Cu–NH_3)^+$ in Cu- CHA [125], and calculated the phase diagram of $Cu(NH_3)_x^+$ in CHA as a function of NH_3 pressure and temperature, as well as the thermodynamics and kinetics of O_2 activation. Moreno-González calculated the entire reaction pathway on Cu-CHA [126] and found that the activation barriers in the direct oxidation of dimers are only 70 kJ/mol. Barriers of over 2 eV were calculated for Cu-SAPO-18 [127].

Recently, metal-organic frameworks, such as manganese- or iron-

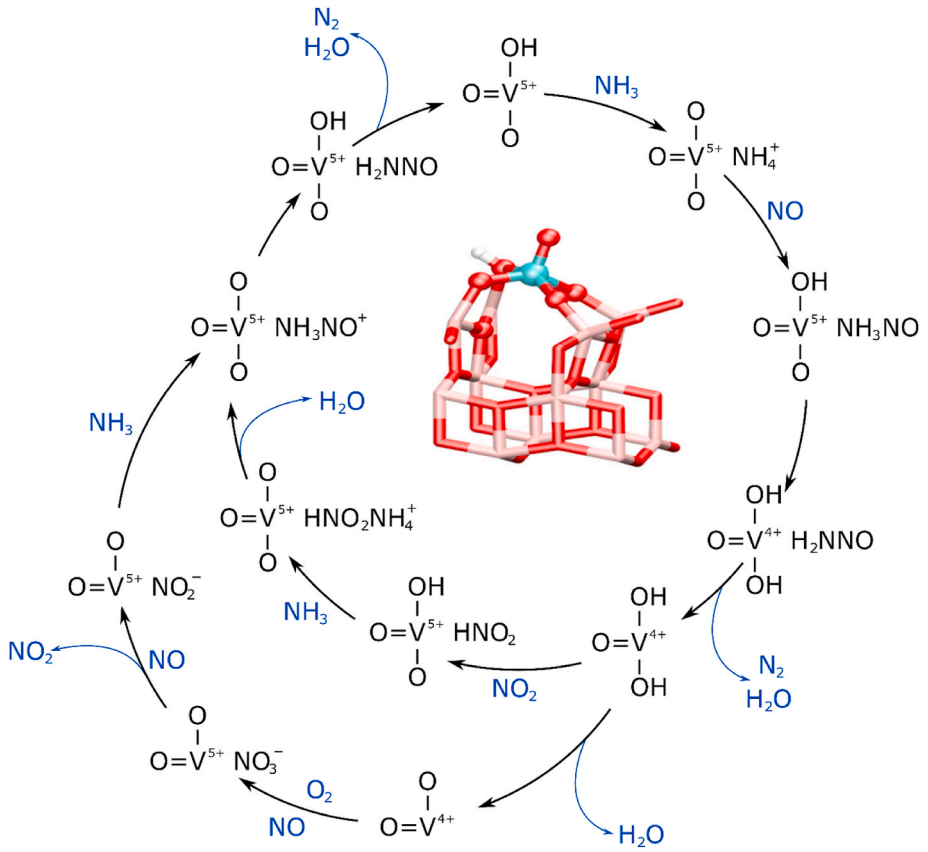

Fig. 3. A reaction mechanism of the SCR process on a VOx/TiO_2 catalyst, as revealed by DFT calculations. Adapted from Ref. [121]. © 2017 Elsevier Inc.

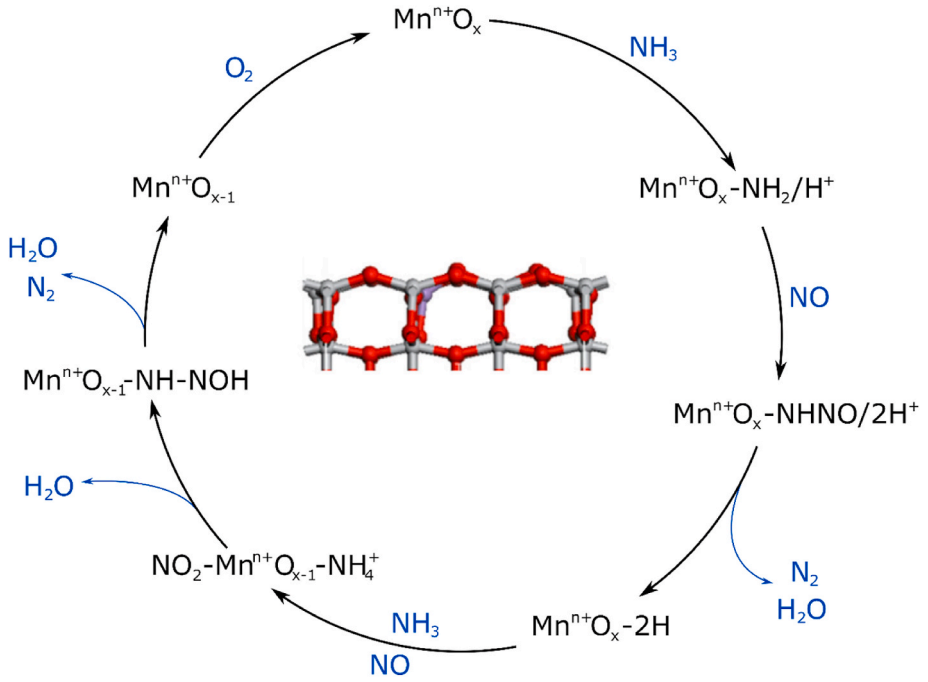

Fig. 4. NH_3-SCR reaction path over $MnOx/TiO_2$ catalyst discovered via DFT calculation. Adapted from Ref. [122]. © 2017 Elsevier B.V.

based BTCs (1,3,5-benzenetricarboxylate), have seen increased interest in mechanistic studies. Song et al. [128] showed computationally that on quasi-Mn-BTC, Eley-Rideal and Langmuir-Hinshelwood mechanisms compete. In the "fast reaction", which proceeds via the LH mechanism, the N–H bond of NH_3 is first cleaved off on a Lewis acid site. Upon a quick formation of NH_2NO, its conversion of HNNOH is the rate-determining step with a barrier of 0.79 eV, which later decomposes to H_2O and N_2. In the "standard mechanism", which follows the ER pathway, the rate determining steps are the formation of NH_2NO from NH_2 and gaseous NO (0.73 eV) and its conversion to HNNOH (0.79 eV).

A similar competition of the two mechanisms was shown for Mn–Fe-BTC, as well [129].

2.3.3. Ceria-based and other oxide catalysts

W-doped CeO_2 was studied by Liu et al. [130], who calculated the entire reaction pathway. Using a simplified four-step catalytic cycle, the effect of W was shown to be beneficial. On $MnCe_{1-x}O_2(111)$, a full mechanistic study revealed that NH_2 forms after the N–H dissociation of ammonia, which then forms NH_2NO upon adsorption of NO. Water desorption was identified as the rate determining step [131]. SO_4^{2-} can promote the reaction, was shown by Zhang et al. [132], who calculated the reaction pathway of NH_3 and NO in the presence of SO_4^{2-}-$CeO_2(111)$ sites.

To investigate SCR on bifunctional V_a-MnO_x catalysts, Xin et al. [133] constructed $Mn_2O_3(202)$ and $Mn_2V_2O_7(\bar{2}01)$ surfaces and investigated the entire reaction pathway, including NH_3 dissociation, the reaction with NO and N_2O. They confirmed that NH_2 plays a crucial role in the reaction. On Mn/γ-Al_2O_3, the calculated reaction rate determining barriers were 471.62, 281.25, and 341.55 kJ/mol [134].

A very thorough investigation of the SCR pathway on α-$Fe_2O_3(012)$ was carried out by Gao et al. [135]. They investigated the standard NH_3-SCR reaction and found that the reaction follows the NO activation mechanism, forming NH_2NO and decomposing it into N_2 and H_2O. The first two are the rate-determining steps with barriers of 1.22 and 1.34 eV.

To recap, density functional theory calculations (DFT) were initially used to obtain the structures and electronic properties of the catalyst and the participating species. This included studying the adsorption of NH_3, NO_2, NO, O_2, N_2 and H_2O. On most catalysts, only NH_3 and H_2O exhibit a strong adsorption, while the other gases physisorb weakly and thus participate in the reaction via the Eley-Rideal mechanism. Rarely, such computations are employed to construct phase diagrams or to understand different IR or Raman spectra. Mechanistic studies have become prominent in the last decade, revealing the rate-determining steps and different pathways. When the calculated barriers range from 20 to 30 kcal/mol, the reactions are fast. In the NO activation mechanism, the formation of NH_2NO is usually the rate determining step, which is followed by a quick decomposition regardless of the catalyst.

3. Global kinetic and microkinetic modelling

For the ammonia SCR deNO_X reaction, most stationary kinetic models generally assume an Eley-Rideal (ER) mechanism, which implies the reaction between adsorbed NH_3 and the gas phase NO. Moreover, the adsorption equilibrium of ammonia and water at the active sites is assumed (competitive adsorption). The expression for the reaction rate considering the equation for site balance is [45]:

$$r = \frac{kK_{NH_3}C_{NH_3}C_{NO}}{1 + K_{NH_3}C_{NH_3} + K_{H_2O}C_{H_2O}} \tag{3.1}$$

where r, k, K_i and C_i are the reaction rate, the intrinsic chemical rate constant, the adsorption equilibrium constant of species i and the gas phase concentration of species i, respectively.

However, adsorption of water on the active sites is usually not considered in kinetic models (see Refs. [136–138].

The other type of kinetic models is based on the Langmuir-Hinshelwood (LH) mechanism, which assumes a bimolecular reaction involving two co-adsorbed molecules (e.g. NH_3 and NO) on the surface. These kinetic models take into account the weak adsorption of the NO molecules on the catalyst surface, which occurs at low temperatures (<200 °C) [136].

3.1. Kinetic models of commercial V_2O_5–WO_3–TiO_2 catalysts

Yun and Kim [46] used the global kinetic model including standard, fast, and NH_3 oxidation reactions with the Langmuir-Hinshelwood (LH) mechanism to predict the conversion of NO_X. The reactions and reaction rate expressions are summarized in Table 1.

The terms in the denominators of the reaction rate expressions in Table 1 take into account the inhibitory effects of surface coverage of the species.

The rate constants (k) and adsorption constants (K) both follow the Arrhenius-type expressions:

$$k_i = a_i e^{\frac{-E_i}{RT}} \tag{3.2}$$

$$K_i = A_i e^{\frac{-E_i}{RT}} \tag{3.3}$$

The authors used the commercial one-dimensional BOOST (AVL) code, as part of the gas exchange and cycle simulation, with the optimized reaction constants [46].

Shin et al. [136] developed a kinetic model for the selective catalytic reduction of nitrogen oxides based on the Eley-Rideal (ER) mechanism, using the equation-based modelling tool gPROMS® ProcessBuilder®.It was employed to evaluate the kinetic model by extracting intrinsic kinetic parameters from the experimental data collected in a conventional fixed-bed reactor. The modelling was performed considering all possible relevant catalytic reactions at SCR catalysts (Table 2), which can be classified into three groups: NO_X reduction (reaction numbers 1–3), NH_3 oxidation (reaction numbers 4–7) and accompanying reactions (gas-phase thermal reactions; reaction numbers 8–10).

NH_3 oxidation with lattice oxygen is expected to occur at relatively high temperatures. The model is a dual-site model: NO and NO_2 were assumed to compete with O_2 for the same adsorption site, while NH_3 adsorbes on a different site, as indicated by the rate expressions in Table 2. The reaction order with respect to O_2 (n) was estimated for the additional homogeneous gas-phase reactions.

The rate (k) and adsorption (K) constants were defined as:

$$k_i = k_{i,T_{ref}} e^{\frac{-E_i}{R}\left(\frac{1}{T}-\frac{1}{T_{ref}}\right)} \tag{3.4}$$

$$K_i = K_{i,T_{ref}} e^{\frac{-\Delta H_i}{R}\left(\frac{1}{T}-\frac{1}{T_{ref}}\right)} \tag{3.5}$$

3.2. Kinetic models of commercial Fe-zeolite catalysts

Metkar et al. [137] performed a comprehensive experimental and modelling study of the selective catalytic reduction of NO_X with NH_3 over Fe-ZSM-5 and Cu-chabazite (CHA) catalysts; only the modelling of SCR of nitrogen oxides over the Fe-ZSM-5 catalyst is described here. They developed a global kinetic model for the NO_X reduction reactions that occur during NH_3-SCR. Their model assumes a first-order dependence on the reactants, with some exceptions e.g. for the standard SCR reaction. The advantage of this model is the smaller number of kinetic parameters, but it lacks a mechanistic sophistication. The chemical reactions and their rate equations are listed in Table 3.

The definition of the rate constants (equation (3.2)) is the same as in the model of Yun and Kim [46].

Ammonia was assumed to adsorb on sites S, which can be considered as Brønsted acid sites. A coverage dependent desorption activation energy was assumed. The denominator in the rate expression for the standard SCR reaction (reaction number 4 in Table 3) explains the observed ammonia inhibition at lower temperatures. It is worth noting that several side reactions produce byproducts. One important byproduct is ammonium nitrate (NH_4NO_3), which is formed in the presence of excess NO_2. The formation of ammonium nitrate is particularly important at lower temperatures (<250 °C). It is assumed that the active sites of the catalyst are either free or have adsorbed ammonia. The rate expressions do not contain an explicit dependence on the concentrations of O_2 and H_2O.

Table 1
Reactions and rate expressions in the global kinetic model of Yun and Kim [46].

Number	Reaction	Rate expression
1	$4NH_3 + 4NO + O_2 \rightarrow 4N_2 + 6H_2O$	$\frac{kC_{NH_3}C_{NO}C_{O_2}}{T(1+K_{NO}C_{NO}+K_{H_2O}C_{H_2O})^2(1+K_{NH_3}C_{NH_3})^2(1+K_{O_2}C_{O_2})^2}$
2	$4NH_3 + 2NO + 2NO_2 \rightarrow 4N_2 + 6H_2O$	$\frac{kC_{NH_3}C_{NO}C_{NO_2}}{T(1+K_{NO}C_{NO}+K_{H_2O}C_{H_2O})^2(1+K_{NH_3}C_{NH_3})^2}$
3	$4NH_3 + 5O_2 \rightarrow 4NO + 6H_2O$	$\frac{kC_{NH_3}C_{NO_2}}{T(1+K_{NO}C_{NO}+K_{H_2O}C_{H_2O})^2(1+K_{NH_3}C_{NH_3})^2(1+K_{O_2}C_{O_2})^2}$

Symbols: T – temperature, A,a - pre-exponential factor, E - activation energy, R - universal gas constant.

Table 2
Reactions and rate expressions in the kinetic model of Shin et al. [136].

Number	Reaction	Rate expression
1	$4NH_3 + 4NO + O_2 \rightarrow 4N_2 + 6H_2O$	$\frac{kK_{NH_3}P_{NH_3}K_{O_2}P_{O_2}P_{NO}}{(1+K_{NH_3}P_{NH_3})(1+K_{O_2}P_{O_2}+K_{NO}P_{NO}+K_{NO_2}P_{NO_2})}$
2	$6NO + 4NH_3 \rightarrow 5N_2 + 6H_2O$	$\frac{kK_{NH_3}P_{NH_3}P_{NO}}{(1+K_{NH_3}P_{NH_3})}$
3	$2NO_2 + 4NH_3 + O_2 \rightarrow 3N_2 + 6H_2O$	$\frac{kK_{NH_3}P_{NH_3}K_{O_2}P_{O_2}P_{NO_2}}{(1+K_{NH_3}P_{NH_3})(1+K_{O_2}P_{O_2}+K_{NO}P_{NO}+K_{NO_2}P_{NO_2})}$
4	$4NH_3 + 3O_2 \rightarrow 2N_2 + 6H_2O$	$\frac{kK_{NH_3}P_{NH_3}K_{O_2}P_{O_2}}{(1+K_{NH_3}P_{NH_3})(1+K_{O_2}P_{O_2}+K_{NO}P_{NO}+K_{NO_2}P_{NO_2})}$
5	$4NH_3 + 5O_2 \rightarrow 4NO + 6H_2O$	$\frac{kK_{NH_3}P_{NH_3}K_{O_2}P_{O_2}}{(1+K_{NH_3}P_{NH_3})(1+K_{O_2}P_{O_2}+K_{NO}P_{NO}+K_{NO_2}P_{NO_2})}$
6	$2NH_3 + 8NO \rightarrow 5N_2O + 3H_2O$	$\frac{kK_{NH_3}P_{NH_3}P_{NO}}{(1+K_{NH_3}P_{NH_3})}$
7	$4NH_3 + 4NO + 3O_2 \rightarrow 4N_2O + 6H_2O$	$\frac{kK_{NH_3}P_{NH_3}K_{O_2}P_{O_2}P_{NO}}{(1+K_{NH_3}P_{NH_3})(1+K_{O_2}P_{O_2}+K_{NO}P_{NO}+K_{NO_2}P_{NO_2})}$
8	$2NO + O_2 \rightarrow 2NO_2$	$k_{i,T_{ref}} e^{\frac{-E_i}{R}\left(\frac{1}{T}-\frac{1}{T_{ref}}\right)} {C_{NO}}^2 {C_{O_2}}^n$
9	$4NH_3 + 5O_2 \rightarrow 4NO + 6H_2O$	$k_{i,T_{ref}} e^{\frac{-E_i}{R}\left(\frac{1}{T}-\frac{1}{T_{ref}}\right)} {C_{NH_3}} {C_{O_2}}^n$
10	$4NH_3 + 3O_2 \rightarrow 2N_2 + 6H_2O$	$k_{i,T_{ref}} e^{\frac{-E_i}{R}\left(\frac{1}{T}-\frac{1}{T_{ref}}\right)} {C_{NH_3}} {C_{O_2}}^n$

Symbols: P_i - partial pressure of species i, T_{ref} - reference temperature, ΔH_i - adsorption enthalpy of species i.

Table 3
Reactions and rate expressions in the global kinetic model of Metkar et al. [137].

Number	Reaction	Rate expression
1	$4NH_3 + S \leftrightarrow NH_3 \sim S$	$k_f X_{NH_3}\theta_v - k_b\theta_{NH_3}$
2	$2NH_3 \sim S + 1.5O_2 \rightarrow N_2 + 3H_2O + 2S$	$k_f X_{O_2}\theta_{NH_3}$
3	$NO + 0.5O_2 \leftrightarrow NO_2$	$k_f {X_{O_2}}^{0.5} X_{NO} - k_b X_{NO_2}$
4	$4NH_3 \sim S + 4NO + O_2 \rightarrow 4N_2 + 6H_2O + 4S$	$\frac{k_f X_{NO}\theta_{NH_3}}{1+\frac{k_f}{k_b}X_{NH_3}}$
5	$2NH_3 \sim S + NO + NO_2 \rightarrow 2N_2 + 3H_2O + 2S$	$k_f X_{NO} X_{NO_2}\theta_{NH_3}$
6	$4NH_3 \sim S + 3NO_2 \rightarrow 3.5N_2 + 6H_2O + 4S$	$k_f X_{NO_2}\theta_{NH_3}$
7	$2NH_3 \sim S + 2NO_2 \rightarrow N_2 + NH_4NO_3 + H_2O + 2S$	$k_f X_{NO_2}\theta_{NH_3}$
8	$NH_4NO_3 \rightarrow N_2O + 2H_2O$	$k_f X_{NH_4NO_3}$
9	$2N_2O \rightarrow 2N_2 + O_2$	$k_f X_{N_2O}$
10	$2NH_3 \sim S + 3N_2O \rightarrow 4N_2 + 3H_2O + 2S$	$k_f X_{N_2O}\theta_{NH_3}$

Symbols: S - ammonia adsorption site, Θ_i - fractional coverage of sites S, Θ_v - fractional coverage of vacant sites S, X_i - mole fraction of species i, k_f - intrinsic chemical rate constant of the forward reaction, k_b - intrinsic chemical rate constant of the reverse reaction.

3.3. Kinetic models of commercial Cu-zeolite catalysts

Colombo et al. [138] developed a dynamic micro-kinetic model of the SCR deNO$_X$ reactions. The rate parameters were estimated from the transient kinetic runs. The dual-site kinetic scheme includes acidic sites (*) for NH_3 adsorption and desorption (coverage is indicated by the symbol Theta) and sites associated with the Cu promoter of the zeolite catalyst (S-sites), where reaction steps (reaction numbers 2–8 in Table 4) involving nitrites/nitrates are expected (coverage is indicated with the symbol sigma).

The kinetic mechanism in Table 4 explicitly accounts for the differences in the formal oxidation state of nitrogen in both gaseous and surface NO_X species. The oxidation state of the catalytic sites (S–OH) is assumed to be invariant because the strong oxidizing conditions associated with the presence of NO_2 likely maintain the Cu-sites in their highest oxidation state.

Additional global reactions were also included in the model to better describe the reaction system: ammonium nitrate formation, sublimation and decomposition to N_2O (reactions 9–11 in Table 4), reversible NO oxidation to NO_2 (reaction 12 in Table 4), and the slow SCR reaction (reaction 13 in Table 4).

It should be noted that all kinetic runs reported in this study were performed in the absence of oxygen in the feed stream to avoid interference with the standard SCR and the NO and ammonia oxidation reactions.

Shibata et al. [139] developed a simple kinetic model for the standard NH_3-SCR reaction with Cu-ZSM-5 catalyst, considering only three reaction steps: NH_3 adsorption (and desorption), NH_3 oxidation and the standard SCR reaction. Their model was validated with the experimental results, which had not been considered in the estimation of the model.

Global kinetic and microkinetic models of SCR deNO$_X$ processes are usually based either on the Eley-Rideal (ER) or on the Langmuir-Hinshelwood (LH) reaction mechanisms. The models usually consider

Table 4
Reactions and rate expressions in the micro-kinetic model of Colombo et al. [138].

Number	Reaction	Rate expression
1	$NH_3 \leftrightarrow {NH_3}^*$	$k_f C_{NH_3}\theta_v - k_b\theta_{NH_3}$
2	$2NO_2 + 2S \sim OH \leftrightarrow S \sim ONO + S \sim NO_3 + H_2O$	$k_f (C_{NO_2}\sigma_v)^2 - k_b\sigma_{ONO}\sigma_{NO_3}$
3	$NO_2 + S \sim ONO \leftrightarrow NO + S \sim NO_3$	$k_f C_{NO_2}\sigma_{ONO} - k_b C_{NO}\sigma_{NO_3}$
4	$S \sim NO_3 + \frac{1}{2}H_2O \rightarrow NO_2 + \frac{1}{4}O_2 + S \sim OH$	$k\sigma_{NO_3}$
5	$S \sim ONO + {NH_3}^* \rightarrow N_2 + H_2O + S \sim OH$	$k\theta_{NH_3}\sigma_{ONO}$
6	$S \sim NO_3 + \frac{2}{3}{NH_3}^* \rightarrow S \sim ONO + \frac{1}{3}N_2 + H_2O$	$k\sigma_{NO_3}\theta_{NH_3}$
7	$S \sim NO_3 + {NH_3}^* \leftrightarrow S \sim NO_3[NH_3]$	$k_f\theta_{NH_3}\sigma_{NO_3} - k_b\sigma_{NO_3[NH_3]}$
8	$S \sim NO_3[NH_3] \rightarrow N_2O + H_2O + S \sim OH$	$k\sigma_{NO_3[NH_3]}$
9	$2{NH_3}^* + 2NO_2 \rightarrow {NH_4NO_3}^* + N_2 + H_2O$	$\frac{k\theta_{NH_3}{C_{NO_2}}^2}{1+K_{NH_4NO_3}\theta_{NH_4NO_3}}$
10	${NH_4NO_3}^* \rightarrow [NH_3 + HNO_3] \rightarrow NH_4NO_3$	$k\theta_{NH_4NO_3}$
11	${NH_4NO_3}^* \rightarrow N_2O + 2H_2O$	$k\theta_{NH_4NO_3}$
12	$NO + \frac{1}{2}O_2 \leftrightarrow NO_2$	$\left\{k\left[C_{NO}(P_{O_2})^{0.5} - \frac{C_{NO_2}}{K_{eq-NO}}\right]\right\}\left(\frac{P_{H_2O}}{0.03}\right)^{\theta}$
13	$\frac{3}{2}NO + {NH_3}^* \rightarrow \frac{5}{4}N_2 + \frac{3}{2}H_2O$	$k\theta_{NH_3}C_{NO}$

Symbols: * - acidic site, S - Cu promoter site, Θ_i - fractional coverage of sites *, σ_i - fractional coverage of S sites, $K_{eq\text{-}NO}$ - chemical equilibrium constant defined in Ref. [138].

one or two types (dual-site models) of adsorption sites and from 3 up to 13 reactions. Some of the studied kinetic models also predict the formation of intermediates in form of nitrites and/or nitrates (e.g. ammonium nitrate). However, most of kinetic models available in the literature do not account for the adsorption of water molecules on the active sites of SCR deNO$_X$ catalysts.

4. CFD simulations

The kinetic model of Shin et al. [136] (described in chapter 3.1.; Table 2) and the estimated parameters were summarized in the form of a user-defined function (UDF) used in a commercial computational fluid dynamics (CFD) package, ANSYS® Fluent®, to search for an optimized SCR monolith channel geometry.

The 3D model of a channel for the SCR honeycomb catalyst had a length of 450 mm (Fig. 5), which is the commonly observed length of commercial SCR monoliths. To save computational time, accounting for the symmetry of the monolith cross-section, only a quarter of the monolith channel was modelled.

The reaction kinetic parameters obtained from the fixed-bed experiments were converted into a surface reaction model, which was applied to the surface zones of the monolith catalyst of the CFD simulation. The gas-phase and the catalytic reaction rate equations were implemented as two UDFs written in C and dynamically linked to the ANSYS Fluent solver.

The CFD calculations were performed with constant velocity inlet boundary conditions for the gas mixture. The outlet pressure was set to the atmospheric pressure. The catalyst wall was set to a constant reaction temperature. The Reynolds numbers of the flow were in the laminar range (500–800).

Square and rectangular channel geometries (with different aspect ratios B/A) were tested for pressure drop and NO conversion (Fig. 7). The width of the channel is denoted by A, while the wall thickness C was kept at 0.7 mm (Fig. 6).

The relative NO conversion and pressure drop on the ordinate axes of Fig. 7 were defined as the ratio of NO conversion and pressure drop of the rectangular channel to those of the square channel. As the aspect ratio of the rectangular channel is increased, both the pressure drop and NO conversion decrease, so there is a tradeoff between these the two factors in choosing the optimal size and geometry of the channel. The aspect ratios that are practical for commercial production are in the range of 1–5 [136].

Since rectangular channels have 90° angles at the corners, they can affect monolith performance by reducing chemical conversion, increasing pressure drop and increasing susceptibility to plugging and scaling (when particles are present in the flue gas stream). To mitigate these problems, an elongated hexagonal channel (with an angle of 120°) was tested using the CFD methodology. With a channel width of 3.2 mm and an aspect ratio of 2.5, the elongated hexagonal channel exibited a 3.5% lower pressure drop while maintaining the same degree of NO conversion. This can be explained by comparing the velocity field distributions in the rectangular and hexagonal channels: the higher portion of the rectangular cross-section has lower velocities than its elongated hexagonal counterpart (under the same boundary conditions). The regions of low flow velocities of the rectangular channel are located near the catalyst surface, resulting in inefficient use of the channel space for catalytic reactions.

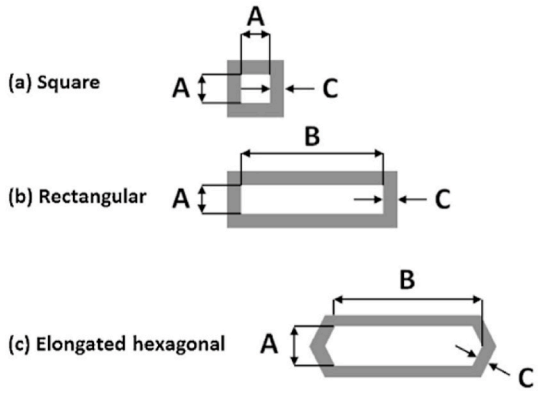

Fig. 6. The tested different monolith cross-sections with symbols (A, B and C) for their characteristic dimensions [136]. © 2019 Institution of Chemical Engineers. Published by Elsevier B.V.

The steady-state application of the NH$_3$-SCR deNO$_X$ process in a coal-fired power plant was modelled considering only the standard SCR reaction and the reaction of ammonia oxidation, which were inserted into the UDF used with the CFD simulation in the ANSYS Fluent software package. The catalyst used was the commercial V_2O_5-WO_3/TiO_2 honeycomb catalyst. Zhou et al. [140] studied the instantaneous velocity distributions and ammonia slip in their 3D model of a SCR system and suggested some changes to the geometry of the elements of the system.

There are not many articles published on the CFD simulations of the NH$_3$-SCR deNO$_X$ process itself. On the other hand, there are many CFD studies [141–143] on the injection of urea-water solution (UWS) into SCR deNO$_X$ systems. Three-dimensional (3D) numerical simulations of vanadia monolith honeycomb catalysts can also be found in the literature. Roduit et al. [144] used finite-element methods programmed in Matlab V to investigate the flow, mass transfer, and chemical reaction processes (Eley-Rideal (ER) mechanism for the standard SCR reaction and the NH$_3$ oxidation side reaction) in a honeycomb catalyst to calculate the distribution of NO concentration in the catalyst wall. Zheng et al. [145] also developed a three-dimensional model combining the selective catalytic reduction (standard SCR reaction) of NO with ammonia and SO_2 oxidation reactions over a monolithic honeycomb catalyst to investigate the effects of catalyst structure and operating parameters on NO reduction and SO_2 oxidation.

The CFD modelling approaches usually incorporate the SCR deNO$_X$ chemical reactions by the user-defined functions (UDFs) and couple them with the mass transport phenomena associated with fluid flow through the monolith catalyst channels. Most of the CFD modelling is done using commercial CFD software packages. The fluid flow conditions are typically in the laminar regime and at least with conventional channel designs there is a trade-off between the pressure drop and the NO$_X$ conversion performance. The literature on CFD modelling of NH$_3$-SCR deNO$_X$ processes is scarce, while there are many CFD studies on the injection of urea-water solution (UWS) into SCR deNO$_X$ systems.

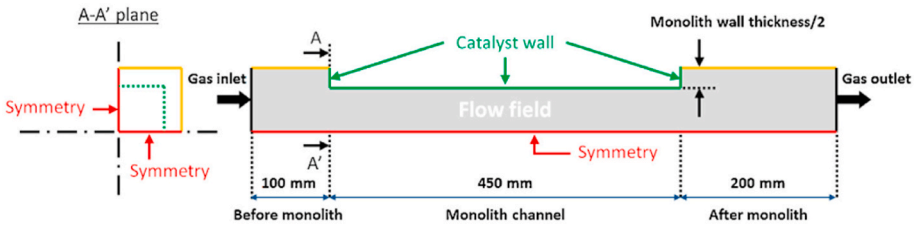

Fig. 5. Schematic representation of the 3D model of the single monolith channel [136]. © 2019 Institution of Chemical Engineers. Published by Elsevier B.V.

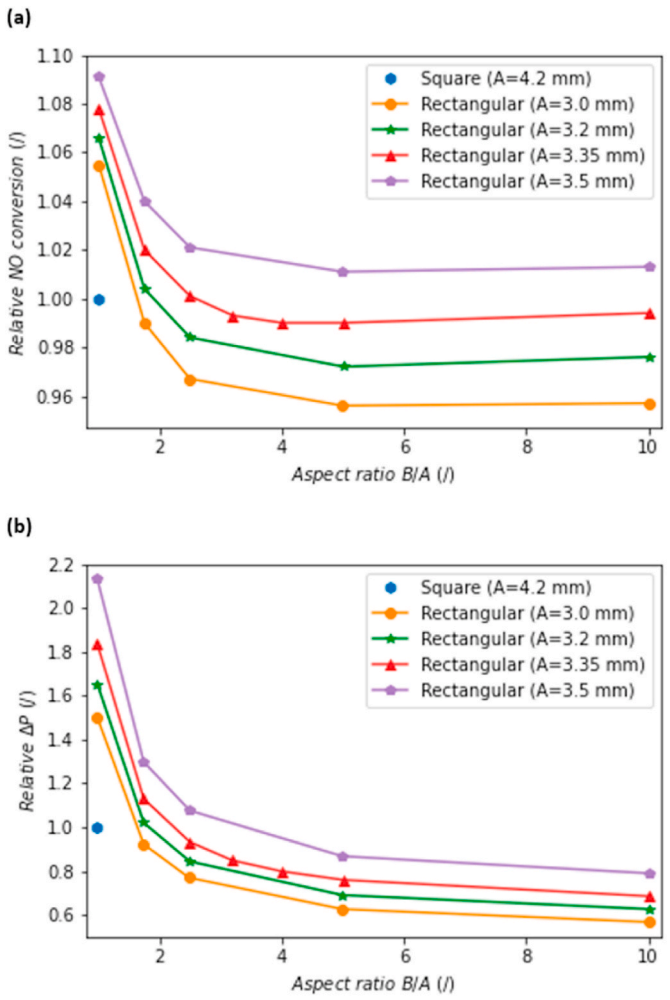

Fig. 7. Performance comparison between a square and a rectangular channel with the same wall thickness (0.7 mm): (a) relative NO turnover and (b) relative pressure drop. Inlet boundary conditions: 1500 ppm NO,1500 ppm NH_3, 0.5 vol % H_2O, 13.5 vol% O_2 and N_2 equilibrium at 5 m/s and 350 °C. Adapted from Ref. [136]. © 2019 Institution of Chemical Engineers. Published by Elsevier B.V.

5. Conclusions

With recent advances in computational methods and available computing power, periodic first-principles models are increasingly being used to gain additional insight into the reaction mechanism. However, most experimental studies still incorporate DFT considerations that are, at best, tentatively linked to the experiments. In most cases, DFT studies deal with adsorption of ammonia and other reactants and products. Comprehensive mechanistic studies that would offer promising insights into reaction mechanism and kinetics remain relatively rare. When they are performed, they are purely theoretical studies with little to no experimental support. This represents an important gap between the state of the art of computations and experimental work, offering a promising avenue for further research. Most importantly, reasonable structural models are essential for high quality and useful DFT calculations. Since the catalyst is an active and constantly changing system during the reaction, this is a daunting task. A naive way to solve this problem is to find an "average" catalyst structure and construct an atomistic approximation of the catalyst structure. While this provides useful results, it is not sufficient to provide a complete mechanistic description of a functioning catalyst.

Nevertheless, the present studies are also useful for catalyst screening for targeted improvement. In the future, the increasing accuracy of DFT studies will allow them to be used for prediction, design and selection of active catalyst materials with desired properties. Here, the resistance to hydroxylation and water poisoning is the most pressing issue, as this has been repeatedly shown to be the rate-determining step in the reaction and thus acts as a bottleneck to the overall catalyst performance.

Most kinetic models in the literature do not account for the adsorption of water molecules on the catalysts. Therefore, it is not possible to predict the conversion performance of the catalysts at higher water vapor content using this group of models. In contrast, the global kinetic model of Yun and Kim [46] considered the adsorption of water vapor on the active sites of the commercial V_2O_5–WO_3–TiO_2 catalyst and showed a significant reduction of the performance in the lower temperature range of the catalyst even at a H_2O content of 10 vol% in the feed gases.

The CFD modelling approach usually considers chemical reactions within the user-defined function/s (UDF/s) and couples it/them with mass transport phenomena associated with the fluid flow through the catalyst, which is done in commercial CFD software packages (e.g. ANSYS Fluent). The development of the detailed CFD methodology could also model processes of adsorption and desorption of species (e.g. ammonia and water) on the catalyst.

During the literature review, the authors identified a large knowledge gap on the topic of NH_3-SCR deNO_X from flue gases with high water vapor content (>15 vol%) produced after hydrogen or ammonia combustion. This gap has been identified in terms of both experimental results and modelling. We see a great need for investigations of the SCR deNO_X process of flue gases with high water content.

The authors would also like to thank the journals that permitted the use of Figs. 1, Fig. 2, Fig. 3, Figs. 4, Fig. 5, Figs. 6 and 7.

Declaration of competing interest

The authors declare that they have no known competing financial interests or personal relationships that could have appeared to influence the work reported in this paper.

Data availability

Data will be made available on request.

Acknowledgements

M.H. appreciates the support from the Slovenian Research Agency through Project N1-0303, Core Funding P2-0421, and Infrastructure Funding I0-0039. B.L. thanks the support from the Slovenian Research Agency through core funding P2-0152 and project funding J7-4638.

Appendix A. Properties of hydrogen and ammonia as fuels

Hydrogen as a fuel has low minimum ignition energy (0.02 mJ), wide ignition limits (4.1–75% in air) and high flame propagation rate (stochiometric laminar flame velocity of 270 cm/s). Therefore, it could be more dangerous than gasoline or natural gas [146]. The adiabatic flame temperature of hydrogen is 2384 K (2111 °C). The average temperature and NO_X emissions in an axisymmetric small burner were 1268 K and 562 ppm, respectively. For conventional combustion of hydrogen, the predicted maximum NO_X was 1961 ppm and the predicted maximum temperature was about 2325 K; therefore, local temperatures and NO_X concentrations vary by site [147]. Hydrogen emits up to 5000 ppm of NO_X [148].

The combustion characteristics of ammonia are: high minimum ignition energy (8 mJ [149]), narrow ignition limits (16–25% by volume in air [150]), low flame propagation rate (laminar flame velocity of 7 cm/s [151]) and relatively low adiabatic flame temperature (lower than hydrogen; 2050 K - 1777 °C [152]). Combustion of ammonia with air produces about 2645 ppm NO_X with an equivalence ratio of 0.94 [153]. Plasma assisted combustion [153] and rich-lean staged combustion [154] can reduce NO_X emissions from ammonia combustion. Ammonia emits up to 2750 ppm of NO_X [148].

Some researchers also studied the combustion of mixtures of the two fuels. The combustion of hydrogen-ammonia mixtures was studied by [155] and [152].

Appendix B. Combustion reactions of hydrogen and ammonia and composition of their combustion products

The heat of combustion of hydrogen under standard conditions is −285.8 kJ/mol, while for ammonia it is −382.8 kJ/mol. The energy density of hydrogen is 141.8 kJ/g or 11.68 kJ/dm^3 (at 101325 Pa, 25 °C), while ammonia has values of 22.48 kJ/g and 15.65 kJ/dm^3 (at 101325 Pa, 25 °C).

$$H_2 + \frac{1}{2}O_2 + 1.881N_2 \rightarrow H_2O + 1.881N_2 \quad \text{(B.1)}$$

$$NH_3 + \frac{3}{4}O_2 + 2.821N_2 \rightarrow \frac{3}{2}H_2O + 3.321N_2 \quad \text{(B.2)}$$

Combustion products at various equivalence ratios (ER) are listed in Tables B1 and B.2. Note that the formation of nitrogen oxides during the combustion of hydrogen and ammonia is not considered here.

Table B.1
Composition of the combustion products after the combustion of hydrogen with air.

ER	H_2 (vol%)	H_2O (vol%)	O_2 (vol%)	N_2 (vol%)
0.75	10.4	31.1	0.0	58.5
0.80	8.0	31.9	0.0	60.1
0.85	5.8	32.7	0.0	61.5
0.90	3.7	33.4	0.0	62.9
0.95	1.8	34.1	0.0	64.1
1.00	0.0	34.7	0.0	65.3
1.05	0.0	33.3	0.8	65.8
1.10	0.0	32.1	1.6	66.3
1.15	0.0	30.9	2.3	66.8
1.20	0.0	29.8	3.0	67.2
1.25	0.0	28.8	3.6	67.6

Symbols: ER - equivalence ratio.

Table B.2
Composition of the combustion products after the combustion of ammonia with air.

ER	NH_3 (vol%)	H_2O (vol%)	O_2 (vol%)	N_2 (vol%)
0.75	6.5	29.1	0.0	64.4
0.80	4.9	29.6	0.0	65.5
0.85	3.5	30.0	0.0	66.5
0.90	2.3	30.4	0.0	67.3
0.95	1.1	30.8	0.0	68.1
1.00	0.0	31.1	0.0	68.9
1.05	0.0	30.0	0.8	69.3
1.10	0.0	29.0	1.4	69.6
1.15	0.0	28.0	2.1	69.9
1.20	0.0	27.1	2.7	70.2
1.25	0.0	26.3	3.3	70.5

Symbols: ER - equivalence ratio.

References

[1] Marocco P, Gandiglio M, Audisio D, Santarelli M. Assessment of the role of hydrogen to produce high-temperature heat in the steel industry. J Clean Prod 2023;388:135969. https://doi.org/10.1016/J.JCLEPRO.2023.135969.

[2] Ren L, Zhou S, Ou X. The carbon reduction potential of hydrogen in the low carbon transition of the iron and steel industry: the case of China. Renew Sustain Energy Rev 2023;171:113026. https://doi.org/10.1016/J.RSER.2022.113026.

[3] Akhtar MS, Khan H, Liu JJ, Na J. Green hydrogen and sustainable development – a social LCA perspective highlighting social hotspots and geopolitical implications of the future hydrogen economy. J Clean Prod 2023;395:136438. https://doi.org/10.1016/J.JCLEPRO.2023.136438.

[4] Maestre VM, Ortiz A, Ortiz I. Challenges and prospects of renewable hydrogen-based strategies for full decarbonization of stationary power applications. Renew Sustain Energy Rev 2021;152:111628.

[5] Berwal P, Kumar S, Khandelwal B. A comprehensive review on synthesis, chemical kinetics, and practical application of ammonia as future fuel for combustion. J Energy Inst 2021;99:273–98. https://doi.org/10.1016/J.JOEI.2021.10.001.

[6] Yapicioglu A, Dincer I. A review on clean ammonia as a potential fuel for power generators. Renew Sustain Energy Rev 2019;103:96–108. https://doi.org/10.1016/J.RSER.2018.12.023.

[7] Lott P, Wagner U, Koch T, Deutschmann O. Hydrogen combustion engines – chances and challenges on the way towards a decarbonized mobility. Chem Ing Tech 2022;94:217–29. https://doi.org/10.1002/CITE.202100155.

[8] Marwaha A, Subramanian KA. Experimental investigations of effects of cycle time on NOx emission in a hydrogen fueled multi-cylinder automotive spark ignition engine. Sustain Energy Technol Assessments 2022;52. https://doi.org/10.1016/j.seta.2022.102203.

[9] Verhelst S, Wallner T. Hydrogen-fueled internal combustion engines. Prog Energy Combust Sci 2009;35:490–527. https://doi.org/10.1016/J.PECS.2009.08.001.

[10] Bao L, Sun B, Luo Q, Li J, Qian D, Ma H, et al. Development of a turbocharged direct-injection hydrogen engine to achieve clean, efficient, and high-power performance. Fuel 2022;324:124713. https://doi.org/10.1016/J.FUEL.2022.124713.

[11] Dinesh MH, Pandey JK, Kumar GN. Study of performance, combustion, and NOx emission behavior of an SI engine fuelled with ammonia/hydrogen blends at various compression ratio. Int J Hydrogen Energy 2022. https://doi.org/10.1016/J.IJHYDENE.2022.05.287.

[12] Brohi EA. Ammonia as fuel for internal combustion engines?. 2014.

[13] Okafor EC, Somarathne KDKA, Hayakawa A, Kudo T, Kurata O, Iki N, et al. Towards the development of an efficient low-NOx ammonia combustor for a micro gas turbine. Proc Combust Inst 2019;37:4597–606. https://doi.org/10.1016/J.PROCI.2018.07.083.

[14] Valera-Medina A, Pugh DG, Marsh P, Bulat G, Bowen P. Preliminary study on lean premixed combustion of ammonia-hydrogen for swirling gas turbine combustors. Int J Hydrogen Energy 2017;42:24495–503. https://doi.org/10.1016/J.IJHYDENE.2017.08.028.

[15] Cappelletti A, Martelli F. Investigation of a pure hydrogen fueled gas turbine burner. Int J Hydrogen Energy 2017;42:10513–23. https://doi.org/10.1016/J.IJHYDENE.2017.02.104.

[16] Hill SC, Smoot LD. Modeling of nitrogen oxides formation and destruction in combustion systems. Prog Energy Combust Sci 2000;26:417–58. https://doi.org/10.1016/S0360-1285(00)00011-3.

[17] Effects of acid rain | US EPA n.d. https://www.epa.gov/acidrain/effects-acid-rain (accessed October 13, 2022).

[18] Reiss R, Anderson EL, Cross CE, Hidy G, Hoel D, McClellan R, et al. Evidence of health impacts of sulfate-and nitrate-containing particles in ambient air. Inhal Toxicol 2007;19:419–49. https://doi.org/10.1080/08958370601174941.

[19] Nitrogen oxides (NOx) emissions — European Environment Agency n.d. https://www.eea.europa.eu/data-and-maps/indicators/eea-32-nitrogen-oxides-nox-emissions-1/assessment.2010-08-19.0140149032-3(accessed January 16, 2023).

[20] EPA Information - photochemical smog — what it means for us. 2004.

[21] Pflieger M, Kroflič A. Acute toxicity of emerging atmospheric pollutants from wood lignin due to biomass burning. J Hazard Mater 2017;338:132–9. https://doi.org/10.1016/J.JHAZMAT.2017.05.023.

[22] Kroflič A, Grilc M, Grgić I. Does toxicity of aromatic pollutants increase under remote atmospheric conditions? Sci Rep 2015;5(1). https://doi.org/10.1038/srep08859. 2015;5:1–5.

[23] Kim KH, Jahan SA, Kabir E, Brown RJC. A review of airborne polycyclic aromatic hydrocarbons (PAHs) and their human health effects. Environ Int 2013;60:71–80. https://doi.org/10.1016/J.ENVINT.2013.07.019.

[24] Laskin A, Laskin J, Nizkorodov SA. Chemistry of atmospheric brown carbon. Chem Rev 2015;115:4335–82.

[25] Zhuang Y, Pavlish JH. Fate of hazardous air pollutants in oxygen-fired coal combustion with different flue gas recycling. Environ Sci Technol 2012;46:4657–65.

[26] Zhu Y, Chen M, Yang Q, Alshwaikh MJM, Zhou H, Li J, et al. Life cycle water consumption for oxyfuel combustion power generation with carbon capture and storage. J Clean Prod 2021;281:124419. https://doi.org/10.1016/J.JCLEPRO.2020.124419.

[27] Cai T, Zhao D, Li X, Shi B, Li J. Mitigating NOx emissions from an ammonia-fueled micro-power system with a perforated plate implemented. J Hazard Mater 2021;401:123848. https://doi.org/10.1016/J.JHAZMAT.2020.123848.

[28] Doppalapudi AT, Azad AK, Khan MMK. Advanced strategies to reduce harmful nitrogen-oxide emissions from biodiesel fueled engine. Renew Sustain Energy Rev 2023;174:113123.

[29] Kim J, Yu J, Lee S, Tahmasebi A, Jeon CH, Lucas J. Advances in catalytic hydrogen combustion research: catalysts, mechanism, kinetics, and reactor designs. Int J Hydrogen Energy 2021;46:40073–104. https://doi.org/10.1016/J.IJHYDENE.2021.09.236.

[30] Javed MT, Irfan N, Gibbs BM. Control of combustion-generated nitrogen oxides by selective non-catalytic reduction. J Environ Manag 2007;83:251–89.

[31] Locci C, Vervisch L, Farcy B, Domingo P, Perret N. Selective non-catalytic reduction (SNCR) of nitrogen oxide emissions: a perspective from numerical modeling. Flow, Turbul Combust 2018;100:301–40.

[32] Kim BS, Jeong H, Bae J, Kim PS, Kim CH, Lee H. Lean NOx trap catalysts with high low-temperature activity and hydrothermal stability. Appl Catal, B 2020;270:118871. https://doi.org/10.1016/J.APCATB.2020.118871.

[33] Kim B-S, Kim PS, Bae J, Jeong H, Kim CH, Lee H. Synergistic effect of Cu/CeO2 and Pt–BaO/CeO2 catalysts for a low-temperature lean NO x trap. Environ Sci Technol 2019;53:2900–7.

[34] Kwak JH, Szanyi J, Peden CHF. Non-thermal plasma-assisted NOx reduction over alkali and alkaline earth ion exchanged Y, FAU zeolites. Catal Today 2004;89:135–41.

[35] Liu Y, Wang J-W, Zhang J, Qi T-T, Chu G-W, Zou H-K, et al. NO x removal by non-thermal plasma reduction: experimental and theoretical investigations. Front Chem Sci Eng 2022;16:1476–84.

[36] Mohan S, Dinesha P, Kumar S. NOx reduction behaviour in copper zeolite catalysts for ammonia SCR systems: a review. Chem Eng J 2020;384:123253. https://doi.org/10.1016/J.CEJ.2019.123253.

[37] Guan Y, Liu Y, Lv Q, Wang B, Che D. Review on the selective catalytic reduction of NOx with H2 by using novel catalysts. J Environ Chem Eng 2021;9. https://doi.org/10.1016/J.JECE.2021.106770.

[38] Yentekakis Iv, Georgiadis AG, Drosou C, Charisiou ND, Goula MA. Selective catalytic reduction of NOx over perovskite-based catalysts using cx hy (Oz), H2 and CO as reducing agents— a review of the latest developments. Nanomaterials 2022;12. https://doi.org/10.3390/NANO12071042.

[39] Liu Z, Chen C, Zhao J, Yang L, Sun K, Zeng L, et al. Study on the NO2 production pathways and the role of NO2 in fast selective catalytic reduction DeNOx at low-temperature over MnOx/TiO2 catalyst. Chem Eng J 2020;379:122288. https://doi.org/10.1016/J.CEJ.2019.122288.

[40] Nova I, Tronconi E. Urea-SCR technology for deNOx after treatment of diesel exhausts. 2014.

[41] Yu C, Hou D, Huang B, Lu M, Peng R, Zhong Z. A MnOx@Eu-CeOx nanorod catalyst with multiple protective effects: strong SO2-tolerance for low temperature DeNOx processes. J Hazard Mater 2020;399:123011. https://doi.org/10.1016/J.JHAZMAT.2020.123011.

[42] Chen L, Si Z, Wu X, Weng D, Wu Z. Effect of water vapor on NH3–NO/NO2 SCR performance of fresh and aged MnOx–NbOx–CeO2 catalysts. J Environ Sci 2015;31:240–7. https://doi.org/10.1016/J.JES.2014.07.037.

[43] Zhao Z, Li E, Qin Y, Liu X, Zou Y, Wu H, et al. Density functional theory (DFT) studies of vanadium-titanium based selective catalytic reduction (SCR) catalysts. J Environ Sci 2020;90:119–37. https://doi.org/10.1016/J.JES.2019.11.008.

[44] Willi R, Roduit B, Koeppel RA, Wokaun A, Baiker A. Selective reduction of NO by NH3 over vanadia-based commercial catalyst: parametric sensitivity and kinetic modelling. Chem Eng Sci 1996;51:2897–902. https://doi.org/10.1016/0009-2509(96)00171-6.

[45] Cybulski A, Moulijn JA. Structured catalysts and reactors. CRC press; 2005.

[46] Yun BK, Kim MY. Modeling the selective catalytic reduction of NOx by ammonia over a Vanadia-based catalyst from heavy duty diesel exhaust gases. Appl Therm Eng 2013;50:152–8. https://doi.org/10.1016/J.APPLTHERMALENG.2012.05.039.

[47] Metkar PS, Balakotaiah V, Harold MP. Experimental and kinetic modeling study of NO oxidation: comparison of Fe and Cu-zeolite catalysts. Catal Today 2012;184:115–28. https://doi.org/10.1016/J.CATTOD.2011.11.032.

[48] He S, Ren J, Cao P. Green Ce-based honeycomb catalyst with excellent water and sulfur dioxide resistances for low-temperature selective catalytic reduction of NOx with ammonia. Process Saf Environ Protect 2022;162:1–16. https://doi.org/10.1016/J.PSEP.2022.02.066.

[49] Gui R, Yan Q, Xue T, Gao Y, Li Y, Zhu T, et al. The promoting/inhibiting effect of water vapor on the selective catalytic reduction of NOx. J Hazard Mater 2022;439. https://doi.org/10.1016/J.JHAZMAT.2022.129665.

[50] Kašpar J, Fornasiero P, Hickey N. Automotive catalytic converters: current status and some perspectives. Catal Today 2003;77:419–49. https://doi.org/10.1016/S0920-5861(02)00384-X.

[51] Alves L, Holz LIV, Fernandes C, Ribeirinha P, Mendes D, Fagg DP, et al. A comprehensive review of NOx and N2O mitigation from industrial streams. Renew Sustain Energy Rev 2022;155:111916.

[52] Dvořák R, Chlápek P, Jecha D, Puchýř R, Stehlík P. New approach to common removal of dioxins and NOx as a contribution to environmental protection. J Clean Prod 2010;18:881–8. https://doi.org/10.1016/J.JCLEPRO.2010.01.024.

[53] Xie X, Peng J, Zhao S, Wang L, Ge R, Wu S, et al. DeNO x characteristics of commercial SCR catalyst regenerated on-line by dry ice blasting in a coal-fired power plant. Ind Eng Chem Res 2022;61:14382–92. https://doi.org/10.1021/ACS.IECR.2C02422/ASSET/IMAGES/LARGE/IE2C02422_0010.JPEG.

[54] Jeon SW, Song I, Lee H, Kim DH. Enhanced activity of vanadia supported on microporous titania for the selective catalytic reduction of NO with NH3: effect of promoters. Chemosphere 2021;275:130105. https://doi.org/10.1016/J.CHEMOSPHERE.2021.130105.

[55] Zhao S, Song K, Zhu J, Ma D, Shi J-W. Gd-Mn-Ti composite oxides anchored on waste coal fly ash for the low-temperature catalytic reduction of nitrogen oxide. Sep Purif Technol 2022;302:122119.

[56] Liu Y, Wang J, Zhu B, Zhou X, Zhou J, Li F, et al. Poisoning mechanism of the coexistence K and SO2 on the deNOx of MnO2/TiO2 catalyst at low temperature. Process Saf Environ Protect 2023;174:135–44.

[57] Liu Y, Liu J, Zhu B, Chen J, Li F, Sun Y. Insight into the micro-mechanism of Co doping to improve the deNOx performance and H2O resistance of β-MnO2 catalysts. Colloids Surf A Physicochem Eng Asp 2023;662:130983.

[58] Zhang S, Zhang B, Liu B, Sun S. A review of Mn-containing oxide catalysts for low temperature selective catalytic reduction of NO x with NH 3: reaction mechanism and catalyst deactivation. RSC Adv 2017;7(42):26226–42.

[59] Fjp Schott, Balle P, Adler J, Kureti S. Reduction of NOx by H2 on Pt/WO3/ZrO2 catalysts in oxygen-rich exhaust. Appl Catal, B 2009;87:18–29. https://doi.org/10.1016/J.APCATB.2008.08.021.

[60] Hahn C, Endisch M, Fjp Schott, Kureti S. Kinetic modelling of the NOx reduction by H2 on Pt/WO3/ZrO2 catalyst in excess of O2. Appl Catal, B 2015;168–169:429–40. https://doi.org/10.1016/J.APCATB.2014.12.033.

[61] Mohammadi A, Farzi A, Thurner C, Klötzer B, Schwarz S, Bernardi J, et al. Tailoring the metal-perovskite interface for promotional steering of the catalytic NO reduction by CO in the presence of H2O on Pd-lanthanum iron manganite composites. Appl Catal, B 2022;307:121160. https://doi.org/10.1016/J.APCATB.2022.121160.

[62] You Y, Chang H, Zhu T, Zhang T, Li X, Li J. The poisoning effects of phosphorus on CeO2-MoO3/TiO2 DeNOx catalysts: NH3-SCR activity and the formation of N2O. Mol Catal 2017;439:15–24. https://doi.org/10.1016/J.MCAT.2017.06.013.

[63] Liang J, Mi Y, Song G, Peng H, Li Y, Yan R, et al. Environmental benign synthesis of Nano-SSZ-13 via FAU trans-crystallization: enhanced NH3-SCR performance on Cu-SSZ-13 with nano-size effect. J Hazard Mater 2020;398:122986. https://doi.org/10.1016/J.JHAZMAT.2020.122986.

[64] Boubnov A, Carvalho HWP, Doronkin DE, Gu T, Gallo E, Atkins AJ, et al. Selective catalytic reduction of NO over Fe-ZSM-5: mechanistic insights by operando HERFD-XANES and valence-to-core X-ray emission spectroscopy. J Am Chem Soc 2014;136:13006–15. https://doi.org/10.1021/ja5062505.

[65] Haber J, Block JH, Delmon B. Methods and procedures for catalyst characterization. In: Handbook of Heterogeneous Catalysis: Online; 2008. p. 1230–58.

[66] Gru W, Kydala Ganesha P, Ellmers I, Pérezpérez Veíez R, Huang H, Bentrup U, et al. Active sites of the selective catalytic reduction of NO by NH 3 over Fe-ZSM-5: combining reaction kinetics with postcatalytic Mo ssbauer spectroscopy at cryogenic temperatures. 2020. https://doi.org/10.1021/acscatal.9b04627.

[67] Rozanska X, Sauer J. Oxidative conversion of C1–C3 alkanes by vanadium oxide catalysts. DFT results and their accuracy. Int J Quant Chem 2008;108:2223–9. https://doi.org/10.1002/QUA.21737.

[68] Yan L, Liu Y, Zha K, Li H, Shi L, Zhang D. Deep insight into the structure-activity relationship of Nb modified SnO2-CeO2 catalysts for low-temperature selective catalytic reduction of NO by NH3. Catal Sci Technol 2017;7:502–14. https://doi.org/10.1039/C6CY02242A.

[69] Mu J, Li X, Sun W, Fan S, Wang X, Wang L, et al. Inductive effect boosting catalytic performance of advanced Fe1-xVxOδ catalysts in low-temperature NH3 selective catalytic reduction: insight into the structure, interaction, and mechanisms. ACS Catal 2018;8:6760–74. https://doi.org/10.1021/ACSCATAL.8B01196.

[70] Nolan M, Grigoleit S, Sayle DC, Parker SC, Watson GW. Density functional theory studies of the structure and electronic structure of pure and defective low index surfaces of ceria. Surf Sci 2005;576:217–29. https://doi.org/10.1016/J.SUSC.2004.12.016.

[71] C Mn-Tj of PC. 2009 undefined. Molecular adsorption on the doped (110) ceria surface, vol. 113. ACS Publications; 2009. p. 2425–32. https://doi.org/10.1021/jp809292u.

[72] Nolan M, Parker SC, Watson GW. Reduction of NO 2 on ceria surfaces. 2006. https://doi.org/10.1021/jp055624b.

[73] Joshi A, Rammohan A, Jiang Y, Ogunwumi S. Density functional theory (DFT) study of the interaction of ammonia with pure and tungsten–doped ceria. J Mol Struct: Theochem 2009;912:73–81. https://doi.org/10.1016/J.THEOCHEM.2009.04.030.

[74] Huang L, Zha K, Namuangruk S, Junkaew A, Zhao X, Li H, et al. Promotional effect of the TiO 2 (001) facet in the selective catalytic reduction of NO with NH 3: in situ DRIFTS and DFT studies. Catal Sci Technol 2016;6:8516–24.

[75] Sun C, Liu H, Chen W, Chen D, Yu S, Liu A, et al. Insights into the Sm/Zr co-doping effects on N2 selectivity and SO2 resistance of a MnOx-TiO2 catalyst for the NH3-SCR reaction. Chem Eng J 2018;347:27–40. https://doi.org/10.1016/J.CEJ.2018.04.029.

[76] HeLian Y, Cui S, Ma X, Wang Y. The effect of tourmaline on the denitration performance of MnOx/TiO2 catalysts and DFT calculation. Mol Catal 2022;525:112289. https://doi.org/10.1016/J.MCAT.2022.112289.

[77] Yan L, Liu Y, Zha K, Li H, Shi L, Zhang D. Scale–activity relationship of MnO x-FeO y nanocage catalysts derived from Prussian blue analogues for low-temperature NO reduction: experimental and DFT studies. ACS Appl Mater Interfaces 2017;9:2581–93.

[78] Peng Y, Li J, Shi W, Xu J, Hao J. Design strategies for development of SCR catalyst: improvement of alkali poisoning resistance and novel regeneration method. Environ Sci Technol 2012;46:12623–9.

[79] Due-Hansen J, Boghosian S, Kustov A, Fristrup P, Tsilomelekis G, Ståhl K, et al. Vanadia-based SCR catalysts supported on tungstated and sulfated zirconia: influence of doping with potassium. J Catal 2007;251:459–73. https://doi.org/10.1016/J.JCAT.2007.07.016.

[80] Yin X, Han H, Gunji I, Endou A, Cheettu Ammal SS, Kubo M, et al. NH3 adsorption on the Brönsted and Lewis acid sites of V2O5 (010): a periodic density functional study. J Phys Chem B 1999;103:4701–6.

[81] Peng Y, Yu W, Su W, Huang X, Li J. An experimental and DFT study of the adsorption and oxidation of NH3 on a CeO2 catalyst modified by Fe, Mn, La and Y. Catal Today 2015;242:300–7. https://doi.org/10.1016/J.CATTOD.2014.04.034.

[82] Maitarad P, Zhang D, Gao R, Shi L, Li H, Huang L, et al. Combination of experimental and theoretical investigations of MnO x/Ce0. 9Zr0. 1O2 nanorods for selective catalytic reduction of NO with ammonia. J Phys Chem C 2013;117:9999–10006.

[83] Lu Z, Müller C, Yang Z, Hermansson K, Kullgren J. SO x on ceria from adsorbed SO2. J Chem Phys 2011;134:184703.

[84] Liu Y, Cen W, Wu Z, Weng X, Wang H. SO2 poisoning structures and the effects on pure and Mn doped CeO2: a first principles investigation. J Phys Chem C 2012;116:22930–7.

[85] Kerkeni B, Berthout D, Berthomieu D, Doronkin DE, Casapu M, Grunwaldt J-D, et al. Copper coordination to water and ammonia in CuII-exchanged SSZ-13: atomistic insights from DFT calculations and in situ XAS experiments. J Phys Chem C 2018;122:16741–55.

[86] Cheng K, Liu B, Song W, Liu J, Chen Y, Zhao Z, et al. Effect of Nb promoter on the structure and performance of iron titanate catalysts for the selective catalytic reduction of NO with NH3. Ind Eng Chem Res 2018;57:7802–10.

[87] Liu J, Meeprasert J, Namuangruk S, Zha K, Li H, Huang L, et al. Facet–activity relationship of TiO2 in Fe2O3/TiO2 nanocatalysts for selective catalytic reduction of NO with NH3: in situ DRIFTs and DFT studies. J Phys Chem C 2017;121:4970–9.

[88] Song I, Lee J, Lee G, Han JW, Kim DH. Chemisorption of NH3 on monomeric vanadium oxide supported on anatase TiO2: a combined DRIFT and DFT study. J Phys Chem C 2018;122:16674–82.

[89] Broclawik E, Góra A, Najbar M. The role of tungsten in formation of active sites for no SCR on the V-W-O catalyst surface — quantum chemical modeling (DFT). J Mol Catal Chem 2001;166:31–8. https://doi.org/10.1016/S1381-1169(00)00462-3.

[90] Peng Y, Li J, Si W, Luo J, Dai Q, Luo X, et al. Insight into deactivation of commercial SCR catalyst by arsenic: an experiment and DFT study. Environ Sci Technol 2014;48:13895–900.

[91] Yu Y, Miao J, He C, Chen J, Li C, Douthwaite M. The remarkable promotional effect of SO2 on Pb-poisoned V2O5-WO3/TiO2 catalysts: an in-depth experimental and theoretical study. Chem Eng J 2018;338:191–201. https://doi.org/10.1016/J.CEJ.2018.01.031.

[92] Peng Y, Li J, Si W, Li X, Shi W, Luo J, et al. Ceria promotion on the potassium resistance of MnOx/TiO2 SCR catalysts: an experimental and DFT study. Chem Eng J 2015;269:44–50. https://doi.org/10.1016/J.CEJ.2015.01.052.

[93] Yi-Zhu P, Wan-Hong M, Man-Ke J, Xiao-Rong Z, Johnson DM, Ying-Ping H. Comparing the degradation of acetochlor to RhB using BiOBr under visible light: a significantly different rate-catalyst dose relationship. Appl Catal, B 2016;181:517–23. https://doi.org/10.1016/J.APCATB.2015.08.002.

[94] Paolucci C, Verma AA, Bates SA, Kispersky VF, Miller JT, Gounder R, et al. Isolation of the copper redox steps in the standard selective catalytic reduction on Cu-SSZ-13. Angew Chem Int Ed 2014;53:11828–33.

[95] Borfecchia E, Lomachenko KA, Giordanino F, Falsig H, Beato P, Soldatov A v, et al. Revisiting the nature of Cu sites in the activated Cu-SSZ-13 catalyst for SCR reaction. Chem Sci 2015;6:548–63.

[96] Schneider WF, Hass KC, Ramprasad R, Adams JB. Cluster models of Cu binding and CO and NO adsorption in Cu-exchanged zeolites. J Phys Chem 1996;100:6032–46.

[97] Schneider WF, Hass KC, Ramprasad R, Adams JB. Density functional theory study of transformations of nitrogen oxides catalyzed by Cu-exchanged zeolites. J Phys Chem B 1998;102:3692–705.

[98] Goodman BR, Schneider WF, Hass KC, Adams JB. Theoretical analysis of oxygen-bridged Cu pairs in Cu-exchanged zeolites. Catal Lett 1998;56:183–8.

[99] Goodman BR, Hass KC, Schneider WF, Adams JB. Cluster model studies of oxygen-bridged Cu pairs in Cu− ZSM-5 catalysts. J Phys Chem B 1999;103:10452–60.

[100] Pérez-Badell Y, Solans-Monfort X, Sodupe M, Montero LA. A DFT periodic study on the interaction between O 2 and cation exchanged chabazite MCHA (M= H+, Na+ or Cu+): effects in the triplet–singlet energy gap. Phys Chem Chem Phys 2010;12:442–52.

[101] Pulido A, Nachtigall P. Correlation between catalytic activity and metal cation coordination: NO decomposition over Cu/zeolites. ChemCatChem 2009;1:449–53.

[102] Goodman BR, Hass KC, Schneider WF, Adams JB. Statistical analysis of Al distributions and metal ion pairing probabilities in zeolites. Catal Lett 2000;68:85–93.

[103] Pulido A, Nachtigall P. Correlation between catalytic activity and metal cation coordination: NO decomposition over Cu/zeolites. ChemCatChem 2009;1:449–53.

[104] Pierloot K, Delabie A, Groothaert MH, Schoonheydt RA. A reinterpretation of the EPR spectra of Cu (II) in zeolites A, Y and ZK4, based on ab initio cluster model calculations. Phys Chem Chem Phys 2001;3:2174–83.

[105] McEwen JS, Anggara T, Schneider WF, Kispersky VF, Miller JT, Delgass WN, et al. Integrated operando X-ray absorption and DFT characterization of Cu–SSZ-13 exchange sites during the selective catalytic reduction of NOx with NH3. Catal Today 2012;184:129–44. https://doi.org/10.1016/J.CATTOD.2011.11.037.

[106] Suzuki K, Sastre G, Katada N, Niwa M. Ammonia IRMS-TPD measurements and DFT calculation on acidic hydroxyl groups in CHA-type zeolites. Phys Chem Chem Phys 2007;9:5980–7.

[107] Lo C, Trout BL. Density-functional theory characterization of acid sites in chabazite. J Catal 2004;227:77–89.

[108] Shah R, Gale JD, Payne MC. The active sites of microporous solid acid catalysts. Phase Transitions 1997;61:67–81.

[109] Shah R, Gale JD, Payne MC. Methanol adsorption in zeolites a first-principles study. J Phys Chem 1996;100:11688–97.

[110] Zhang M, Huang X, Chen Y. DFT insights into the adsorption of NH 3-SCR related small gases in Mn-MOF-74. Phys Chem Chem Phys 2016;18:28854–63.

[111] Chen S, Vasiliades MA, Yan Q, Yang G, Du X, Zhang C, et al. Remarkable N2-selectivity enhancement of practical NH3-SCR over Co0. 5Mn1Fe0. 25Al0. 75Ox-LDO: the role of Co investigated by transient kinetic and DFT mechanistic studies. Appl Catal, B 2020;277:119186.

[112] Jia Y, Jiang J, Zheng R, Guo L, Yuan J, Zhang S, et al. Insight into the reaction mechanism over PMoA for low temperature NH3-SCR: a combined In-situ DRIFTs and DFT transition state calculations. J Hazard Mater 2021;412:125258. https://doi.org/10.1016/J.JHAZMAT.2021.125258.

[113] Fan Z, Wang Z, Shi J-W, Gao C, Gao G, Wang B, et al. Charge-redistribution-induced new active sites on (0 0 1) facets of α-Mn2O3 for significantly enhanced selective catalytic reduction of NOx by NH3. J Catal 2019;370:30–7.

[114] Gao C, Xiao B, Shi J-W, He C, Wang B, Ma D, et al. Comprehensive understanding the promoting effect of Dy-doping on MnFeOx nanowires for the low-temperature NH3-SCR of NOx: an experimental and theoretical study. J Catal 2019;380:55–67.

[115] Song K, Gao C, Lu P, Ma D, Cheng Y, Shi J-W. Bimetallic modification of MnFeOx nanobelts with Nb and Nd for enhanced low-temperature de-NOx performance and SO2 tolerance. Fuel 2023;331:125861.

[116] Anstrom M, Topsøe NY, Dumesic JA. Density functional theory studies of mechanistic aspects of the SCR reaction on vanadium oxide catalysts. J Catal 2003;213:115–25. https://doi.org/10.1016/S0021-9517(02)00031-3.

[117] Soyer S, Uzun A, Senkan S, Onal I. A quantum chemical study of nitric oxide reduction by ammonia (SCR reaction) on V2O5 catalyst surface. Catal Today 2006;118:268–78. https://doi.org/10.1016/J.CATTOD.2006.07.033.
[118] Vittadini A, Casarin M, Selloni A. First principles studies of Vanadia− titania monolayer catalysts: mechanisms of NO selective reduction. J Phys Chem B 2005;109:1652–5.
[119] Calatayud M, Mguig B, Minot C. Modeling catalytic reduction of NO by ammonia over V2O5. Surf Sci Rep 2004;55:169–236. https://doi.org/10.1016/J.SURFREP.2004.05.002.
[120] Arnarson L, Falsig H, Rasmussen SB, Lauritsen J v, Moses PG. A complete reaction mechanism for standard and fast selective catalytic reduction of nitrogen oxides on low coverage VOx/TiO2 (0 0 1) catalysts. J Catal 2017;346:188–97.
[121] He G, Lian Z, Yu Y, Yang Y, Liu K, Shi X, et al. Polymeric vanadyl species determine the low-temperature activity of V-based catalysts for the SCR of NO x with NH3. Sci Adv 2018;4:eaau4637.
[122] Wei L, Cui S, Guo H, Ma X. Study on the role of Mn species in low temperature SCR on MnOx/TiO2 through experiment and DFT calculation. Mol Catal 2018;445:102–10. https://doi.org/10.1016/J.MCAT.2017.11.022.
[123] Yuan R-M, Fu G, Xu X, Wan H-L. Brønsted-NH4+ mechanism versus nitrite mechanism: new insight into the selective catalytic reduction of NO by NH3. Phys Chem Chem Phys 2011;13:453–60.
[124] Li J, Li S. A DFT study toward understanding the high activity of Fe-Exchanged zeolites for the “fast” selective catalytic reduction of nitrogen oxides with ammonia. J Phys Chem C 2008;112:16938–44.
[125] Chen L, Falsig H, Janssens TVW, Grönbeck H. Activation of oxygen on (NH3CuNH3)+ in NH3-SCR over Cu-CHA. J Catal 2018;358:179–86.
[126] Moreno-González M, Millán R, Concepción P, Blasco T, Boronat M. Spectroscopic evidence and density functional theory (DFT) analysis of low-temperature oxidation of Cu+ to Cu2+ NO x in Cu-CHA catalysts: implications for the SCR-NO x reaction mechanism. ACS Catal 2019;9:2725–38.
[127] Li Y, Deng J, Song W, Liu J, Zhao Z, Gao M, et al. Nature of Cu species in Cu–SAPO-18 catalyst for NH3–SCR: combination of experiments and DFT calculations. J Phys Chem C 2016;120:14669–80.
[128] Song K, Guo K, Mao S, Ma D, Lv Y, He C, et al. Insight into the Origin of excellent SO2 tolerance and de-NO x performance of quasi-Mn-BTC in the low-temperature catalytic reduction of nitrogen oxide. ACS Catal 2023;13:5020–32.
[129] Song K, Guo K, Lv Y, Ma D, Cheng Y, Shi J-W. Rational regulation of reducibility and acid site on Mn–Fe–BTC to achieve high low-temperature catalytic denitration performance. ACS Appl Mater Interfaces 2023;15:4132–43.
[130] Liu B, Liu J, Ma S, Zhao Z, Chen Y, Gong X-Q, et al. Mechanistic study of selective catalytic reduction of NO with NH3 on W-doped CeO2 catalysts: unraveling the catalytic cycle and the role of oxygen vacancy. J Phys Chem C 2016;120:2271–83.
[131] Song W, Liu J, Zheng H, Ma S, Wei Y, Duan A, et al. A mechanistic DFT study of low temperature SCR of NO with NH 3 on MnCe 1− x O 2 (111). Catal Sci Technol 2016;6:2120–8.
[132] Zhang Y, Zhang K, Yang C, Yang M, Peng G, Xie Y, et al. The promoting mechanism of SO42− on CeO2 for selective catalytic reduction of NO by NH3: a DFT study. Theor Chem Acc 2022;141:1–15.
[133] Xin Y, Li H, Zhang N, Li Q, Zhang Z, Cao X, et al. Molecular-level insight into selective catalytic reduction of NO x with NH3 to N2 over a highly efficient bifunctional V a-MnO x catalyst at low temperature. ACS Catal 2018;8:4937–49.
[134] Li X, Li Q, Zhong L, Song Z, Yu S, Zhang C, et al. DFT analysis of the reaction mechanism for NH3-SCR of NO x over Mn/γ-Al2O3 catalyst. J Phys Chem C 2019;123:25185–96.
[135] Gao M, He G, Zhang W, Du J, He H. Reaction pathways of the selective catalytic reduction of NO with NH3 on the α-Fe2O3 (012) surface: a combined experimental and DFT study. Environ Sci Technol 2021;55:10967–74.
[136] Shin SB, Skau KI, Menon M, Maroor S, Spatenka S. A modelling approach to kinetics study and novel monolith channel design for selective catalytic reduction (SCR) applications. Chem Eng Res Des 2019;142:412–28. https://doi.org/10.1016/J.CHERD.2018.12.029.
[137] Metkar PS, Harold MP, Balakotaiah V. Experimental and kinetic modeling study of NH3-SCR of NOx on Fe-ZSM-5, Cu-chabazite and combined Fe- and Cu-zeolite monolithic catalysts. Chem Eng Sci 2013;87:51–66. https://doi.org/10.1016/J.CES.2012.09.008.
[138] Colombo M, Nova I, Tronconi E. Detailed kinetic modeling of the NH3–NO/NO2 SCR reactions over a commercial Cu-zeolite catalyst for Diesel exhausts after treatment. Catal Today 2012;197:243–55. https://doi.org/10.1016/J.CATTOD.2012.09.002.
[139] Shibata G, Eijima W, Koiwai R, Shimizu K ichi, Nakasaka Y, Kobashi Y, et al. NH3-SCR by monolithic Cu-ZSM-5 and Cu-AFX catalysts: kinetic modeling and engine bench tests. Catal Today 2019;332:59–63. https://doi.org/10.1016/J.CATTOD.2018.06.023.
[140] Zhou Z, Chang J, Wang X. Large eddy simulation of hydrodynamics and deNOx process in a coal-fired power plant SCR system. J Environ Manag 2022:320. https://doi.org/10.1016/J.JENVMAN.2022.115800.
[141] Birkhold F, Meingast U, Wassermann P, Deutschmann O. Modeling and simulation of the injection of urea-water-solution for automotive SCR DeNOx-systems. Appl Catal, B 2007;70:119–27.
[142] Birkhold F, Meingast U, Wassermann P, Deutschmann O. Analysis of the injection of urea-water-solution for automotive SCR DeNOx-systems: modeling of two-phase flow and spray/wall-interaction. SAE Trans 2006:252–62.
[143] Jeong S-J, Lee C-H. A study on the injection characteristics of urea solution to improve deNOx performance of urea-SCR catalyst in a heavy duty diesel engine. Trans Kor Soc Automot Eng 2008;16:165–72.
[144] Roduit B, Baiker A, Bettoni F, Baldyga J, Wokaun A. 3-D modeling of SCR of NOx by NH3 on vanadia honeycomb catalysts. AIChE J 1998;44:2731–44.
[145] Zheng C, Xiao L, Qu R, Liu S, Xin Q, Ji P, et al. Numerical simulation of selective catalytic reduction of NO and SO2 oxidation in monolith catalyst. Chem Eng J 2019;361:874–84.
[146] Das LM. Hydrogen-oxygen reaction mechanism and its implication to hydrogen engine combustion. Int J Hydrogen Energy 1996;21:703–15. https://doi.org/10.1016/0360-3199(95)00138-7.
[147] Ilbas M, Yilmaz I, Veziroglu TN, Kaplan Y. Hydrogen as burner fuel: modelling of hydrogen-hydrocarbon composite fuel combustion and NOx formation in a small burner. Int J Energy Res 2005;29:973–90. https://doi.org/10.1002/er.1104.
[148] Saleem A, Karimi IA, Farooq S. Estimating NOx emissions of useful two-fuel blends from literature data. Fuel 2022;316:123213. https://doi.org/10.1016/J.FUEL.2022.123213.
[149] Verkamp FJ, Hardin MC, Williams JR. Ammonia combustion properties and performance in gas-turbine burners. Symp (Int) on Combust 1967;11:985–92. https://doi.org/10.1016/S0082-0784(67)80225-X.
[150] Gross CW, Kong SC. Performance characteristics of a compression-ignition engine using direct-injection ammonia–DME mixtures. Fuel 2013;103:1069–79. https://doi.org/10.1016/J.FUEL.2012.08.026.
[151] Hayakawa A, Goto T, Mimoto R, Arakawa Y, Kudo T, Kobayashi H. Laminar burning velocity and Markstein length of ammonia/air premixed flames at various pressures. Fuel 2015;159:98–106. https://doi.org/10.1016/J.FUEL.2015.06.070.
[152] Otomo J, Koshi M, Mitsumori T, Iwasaki H, Yamada K. Chemical kinetic modeling of ammonia oxidation with improved reaction mechanism for ammonia/air and ammonia/hydrogen/air combustion. Int J Hydrogen Energy 2018;43:3004–14. https://doi.org/10.1016/J.IJHYDENE.2017.12.066.
[153] Choe J, Sun W, Ombrello T, Carter C. Plasma assisted ammonia combustion: simultaneous NOx reduction and flame enhancement. Combust Flame 2021;228:430–2. https://doi.org/10.1016/J.COMBUSTFLAME.2021.02.016.
[154] Li Z, Li S. Effects of inter-stage mixing on the NOx emission of staged ammonia combustion. Int J Hydrogen Energy 2022;47:9791–9. https://doi.org/10.1016/J.IJHYDENE.2022.01.050.
[155] Li J, Huang H, Kobayashi N. Study on using hydrogen and ammonia as fuels: combustion characteristics and NOx formation. ZH-I journal of, 2014 undefined Wiley Online Libr 2014;vol. 38:1214–23. https://doi.org/10.1002/er.3141.